Intrasalt Structure and Strain Partitioning in Layered Evaporites: Implications for Drilling Through Messinian Salt in the Eastern Mediterranean

Sian L. Evans* and C. A-L. Jackson

Basins Research Group (BRG)
Department of Earth Science and Engineering
Imperial College London
Prince Consort Road
London, SW7 2BP
*sian.evans15@imperial.ac.uk

Abstract

We use 3D seismic reflection data from the Levant margin, offshore Lebanon to investigate the structural evolution of the Messinian evaporite sequence, and how intrasalt strain varies within a thick salt sheet during early-stage salt tectonics. Intra-Messinian reflectivity reveals lithological heterogeneity within the otherwise halite-dominated sequence. This leads to rheological heterogeneity, with the different mechanical properties of the various units controlling strain accommodation within the deforming salt sheet. We assess the distribution and orientation of structures, and show how intrasalt strain varies both laterally and vertically along the margin. We argue that units appearing weakly strained in seismic data, may in fact accommodate considerable sub-seismic or cryptic strain. We also argue that the intrasalt stress state varies through time and space in response to the gravitational forces driving deformation. We conclude that efficient drilling through thick, heterogeneous salt requires a holistic understanding of the mechanical and kinematic development of the salt and its overburden. This will also enable us to build better velocity models that account for intrasalt lithological and structural complexity in order to accurately image sub-salt geological structures.

1 Introduction

Thick salt deposits have a dramatic effect on the subsequent structural evolution of a basin due to their unique ability to behave as a fluid on geological timescales, and thus to flow in response to gravitational driving forces (e.g. Jackson et al., 1994; Jackson, 1995; Hudec and Jackson, 2007; Jackson and Hudec, 2017). The interaction between sedimentation and salt deformation can lead to extreme structural complexity in salt-influenced basins, which presents unique challenges when exploring for and producing hydrocarbons from the subsurface (e.g. Quirk et al., 2012).

Advances in seismic imaging have revolutionised our understanding of the way in which overburden rocks are deformed by flowing salt. However, due to its characteristic chaotic and transparent appearance in seismic reflection data, the internal composition and kinematics of salt bodies have been overlooked. Salt is frequently thought of as a homogeneous body composed of pure halite, but exposures of salt in mines (e.g. Balk, 1949; Hoy et al., 1962; Kupfer, 1962; Miralles et al., 2001; Schleder et al., 2008; Burliga et al., 2018) and in the field (e.g. Zak and Freund, 1980; Jackson et al., 1990; Talbot, 1998), as well as geophysical subsurface data (Van Gent et al., 2011; Strozyk et al., 2012; Jackson et al., 2015; Raith et al., 2016), show that most evaporitic sequences are in fact lithologically heterogeneous (Fig. 1) (see also Rowan et al., 2019). Despite this, the impact of this lithological heterogeneity on the resulting intrasalt deformation and structural evolution is poorly understood.

The young Messinian (latest Miocene) salt giant in the Mediterranean provides a perfect natural laboratory to study active, early-stage salt tectonics of a thick, lithologically heterogeneous salt sheet. The Messinian Salinity Crisis (MSC) is a remarkable geological event that occurred between 5.96 and 5.33 Ma (e.g. Gautier et al., 1994; Ryan, 2009; Roveri et al., 2014). During this time, the Mediterranean Sea was isolated from the Atlantic due to the closure of the Gibraltar Straits, causing rapid evaporitic drawdown and extensive salt precipitation. This resulted in the widespread deposition of a thick (up to 2 km), layered evaporite unit across much of the Mediterranean basin. When the Straits reopened in the Pliocene, the Mediterranean was flooded by marine Atlantic waters, and a clastic overburden (up to 1.5 km thick) was deposited above the salt. Tectonically-driven tilting of the basin margins, as well as differential loading of the salt by prograding clastic wedges, triggered gravity-driven deformation of the Messinian salt, resulting in the development of kinematically-linked zones of updip extension and downdip contraction (Fig. 2) (Cartwright and Jackson, 2008; Gvirtzman et al., 2013; Allen et al., 2016). Salt-related deformation in the Levantine Basin is thought to be dominantly driven by gravity gliding in the north (due to tilting of the margin), and by gravity spreading in the south (due to loading of the salt where the Nile delta is prograding into the basin) (Allen et al., 2016). This gravity-driven deformation of the salt remains active to the present day.

In recent years the eastern Mediterranean region has attracted renewed interest from petroleum explorers. Following the Zohr discovery in 2015, the proven pre-salt plays have become the focus of intense exploration efforts (Esestime et al., 2016). Accurate seismic imaging of the subsalt geology is necessary to successfully target prospects in the pre-salt. Velocity models must therefore consider the complex lithological heterogeneity and internal structure of the Messinian salt. Furthermore, determining the stress state within the deforming salt sheet is important for safe and efficient drilling through the thick, actively flowing salt. For example, Weijermars and Jackson (2014) show that wells drilling through thick salt are at greater risk of lost time and are overall costlier, primarily due to issues related to wellbore stability. Many of these issues could be mitigated by planning well paths that account for the present and likely future stress state within the salt. However, due to typically poor seismic imaging within thick salt, and a lack of outcrop and well data, there have been relatively few studies to constrain the relationship between the intrasalt stratigraphy, structure and the evolution of stress and strain within the deforming salt sheet.

Furthermore, the few previous studies investigating Messinian intrasalt deformation have yielded contradictory results. Cartwright et al. (2012) calculate strain on intrasalt layers using seismic data from offshore Israel (Fig. 2) and interpret an asymmetric Poiseuille flow profile, suggesting a dominantly pressure-induced flow (Fig. 3a). In contrast, Cartwright et al. (2018) and Kirkham et al., (2019) more recently identified deformed gas pipes within the salt in the deep Levantine Basin (Fig. 2), which if taken as direct kinematic indicators suggest a Couette flow profile, indicative of drag-induced flow (Fig. 3b). In this study, we use a 3D seismic reflection dataset located offshore Lebanon in the northern Levantine Basin (Fig. 2) to investigate how intrasalt structure and strain develop within thick salt during the early phase of evaporite deformation. We compare our results to those arising from previous studies and thus attempt to resolve existing contradictions regarding intrasalt flow. Insights gathered from the Mediterranean can also be used to develop our understanding of intrasalt structure and kinematics in other salt-influenced basins around the world.

2 Data and Methods

Because the Messinian evaporite sequence is young, shallow, and only weakly deformed, it is well-imaged by seismic reflection data. The large (c. 10,000 km^2) 3D seismic reflection dataset used in this study is located offshore Lebanon (Fig. 2). It has near-zero phase with reverse polarity, i.e. an increase in acoustic impedance (hard kick) corresponds to a negative amplitude, coloured red (a trough), while a decrease in acoustic impedance (soft kick) corresponds to a positive amplitude, coloured black/blue (a peak). The seismic data are presented in two-way-time (TWT) and dimensions quoted in ms TWT are estimated in equivalent depth using velocities given by Reiche et al. (2014) and Feng et al. (2016) for the intrasalt units and overburden. The vertical resolution (λ/4) of the Messinian interval is estimated to be 16.8 m using an average velocity of 4200 m/s, but this varies with precise composition. In this study we investigate the nature and distribution of intrasalt and supra-salt deformation by mapping intrasalt reflections and seismic facies within the Messinian salt, analysing stratigraphic relationships within the salt and overburden, generating structure maps, and measuring intrasalt strain.

Reflections within the Messinian evaporite sequence allow us to measure strain at different levels within the deforming salt sheet. We follow Cartwright et al. (2012) and calculate the strain along mapped intrasalt reflections on a series of seismic cross-sections through the contractional domain (dominated by reverse shear zones and related folds; this allows us to examine how strain varies horizontally and vertically across the study area. 2D sections are taken perpendicular to the dominant structural trend (NNE-SSW), which is thus parallel to the direction of bulk salt flow (WNW). Strain is calculated using simple line-length analysis on individual reflections (i.e. change in line length divided by original line length; Fig. 4). Line-length analysis measures the total undeformed length of the same horizon, and thus only includes deformation due to seismically-resolved faulting and folding. A similar approach to calculating strain has been previously applied in many different tectonic settings, both with and without salt, using seismic data and/or analogue models (e.g. Cartwright et al., 2012; Burberry, 2015; Coleman et al., 2017; Butler and Paton, 2010; Steventon et al., 2019). This method assumes plane strain deformation and preservation of bed lengths and areas, and thus provides a minimum estimate of shortening. It does *not* include tectonic layer-parallel compaction, which would thicken the layers prior to thrusting and folding. Where reflections are truncated by the overburden, we extrapolate them to where they would intersect with the projected shear zone plane (e.g. Fig. 9). This introduces greater uncertainty in the uppermost layers, but the resulting trends are consistent with those observed even where the evaporite sequence is fully preserved. We therefore design this study to analyse and interpret relative, rather than absolute, values in strain magnitude. Since the measurements of bed-length are dominantly sub-horizontal, lateral velocity variations would not impact these significantly and so the vertical axis of the seismic data is given in two-way-time (TWT). We conclude our study by comparing our results to previous seismic-based studies of intrasalt strain distribution, and integrating observations from exposures of compositionally analogous deformed evaporites.

3 Geological Setting

The East Mediterranean Basin comprises two sub-basins; the Levantine Basin to the east and the Herodotus Basin to the west, separated by the Eratosthenes Seamount (Fig. 2). The basins contain up to 20 km of clastic material overlying thin, oceanic crust (Aal et al., 2000). The seismic data used in this study is situated offshore Lebanon, on the eastern passive margin of the Levantine Basin (Fig. 2).

The eastern Mediterranean is a tectonically complex region. Ongoing convergence between the northward-migrating African plate and the stable Eurasian plate gives rise to active subduction zones along the northern and western basin margins (Ben-Avraham, 1978). The deformation front of the Cyprus Arc, dominated by the Latakia Ridge, forms the northern boundary, in a location where remnant Tethyan oceanic crust is being subducted (Hall et al., 2005). The eastern extension of the Hellenic Arc, forming an accretionary wedge known as the Mediterranean Ridge, bounds the basin to the west.

The Levant passive margin provides the eastern limit to the basin (Hawie et al., 2013). N-S oriented strike-slip faulting occurs onshore in association with the Dead Sea Transform Zone, and the northwards motion of the Arabian plate relative to the African plate. The north African passive margin forms the southern boundary, where the Nile river system is draining the African continental interior and supplying large quantities of clastic material to the basin. The Nile Delta is therefore rapidly prograding northward out into the basin.

The present structure of the basin thus records the complex interplay of thick-skinned tectonic processes related to the geodynamic boundary conditions, and thin-skinned tectonics due to the gravitationally-driven flow of the Messinian evaporites.

4 Margin Characterisation

In this section we focus on characterising the structure and stratigraphy of the salt and overburden imaged in the present dataset. In the proceeding section we then integrate these observations to present an interpretation of the salt tectonics.

4.1 Sub-Salt Structure

The base-salt surface dips predominantly to the NW but the precise dip direction rotates laterally along the margin, from a more WNW dip in the northern part of the study area to a more NNW dip at the southern edge of the study area (Figs 5 and 6). This margin geometry is the structurally shallow expression of the Saida-Tyr Platform, also known as the Levant Ramp; a SW-trending, inversion-related high that extends from the Levant margin into the deep basin, and which was formed during Late Cretaceous continental collision (Nader et al., 2018; Hodgson, 2012).

Where the shelf edge protrudes into the basin in the south, the upper shelf plateau is incised by several Messinian (or post-Messinian) canyons (Fig. 6). Similar features have been described on the southern Levant margin, offshore Israel, where they are inferred to provide evidence for sea level drawdown during the Messinian Salinity Crisis (e.g. Bertoni and Cartwright, 2007). The Latakia Ridge crosses the northwestern corner of the dataset and is expressed as a large, arcuate, broadly NE-trending anticline on both the base-salt and top-salt surfaces (Figs 6 and 7).

A series of NW-SE-striking, relatively short (up to 6 km) and small-displacement (c. 30-60 ms TWT or c. 45-60 m) normal faults offset the base-salt in the deeper basin (Fig. 6). In cross-section these appear to be layer-bound, sub-salt restricted normal faults that terminate at the base-salt. These faults have been interpreted as syn-sedimentary, active during the late Miocene, and are attributed to an anisotropic extensional stress field (Ghalayini et al. 2017; Reiche et al, 2014).

Other features of particular interest on the base-salt surface include the prominent NE-trending anticlines that have relief of up to 650 ms (c. 1 km) (Fig. 6). The folds are 8-28 km long and 2-3 km wide. These features are definitively not salt-related velocity pull-ups (i.e. geophysical artefacts) given that the salt is thinner (as opposed to thicker) over their crests. These anticlines initially formed during the Late Miocene due to NW-SE regional tectonic compression, prior to the Messinian Salinity Crisis, though it is possible they may have been amplified during later shortening (Ghalayini et al. 2014).

4.2 Supra-Salt Structure

Normal faults and reactive diapirs dominate the updip edge of the margin, delineating an extensional regime, although the type and orientation of extensional structures vary along the margin (Figs 5 and

7). In the northern part of the study area, supra-salt extension is accommodated by a polygonal network of mature reactive diapirs and salt rollers (Fig. 7). The reactive diapirs have a characteristic triangular shape in cross-section and are associated with inward-dipping normal faults across their crests (Fig. 8). This style of diapirism contrasts markedly with the southern part of the study area, where extension is accommodated by salt-detached normal faults, sometimes associated with small salt rollers, that are parallel or sub-parallel to the NE-oriented margin. Mature, high-relief reactive diapirs are absent in the south of the present dataset (Fig. 7). Further south along the margin, offshore Israel, high-relief reactive diapirs are also absent in the extensional domain; only salt rollers occur. The reactive, high-relief diapirs therefore appear to be a relatively localised feature along the Levantine margin. However, similar diapiric structures have been documented around the circum-Nile deformation belt (CNDB) (e.g. Allen et al., 2016), and in the equivalent Messinian basins of the western Mediterranean (e.g. Gulf of Lions; dos Reis et al., 2005). The polygonal distribution of these structures seems to suggest that the local differential stress (σ2 - σ3) in this area is small, and as such the structures show no preferred alignment.

The NNE-SSW-striking faults and rollers in the North rotate towards the south to strike broadly WNW-ESE (Fig. 7), closely following the local orientation of the shelf edge and salt pinch-out (Fig 10a). In the far south a few faults even assume a perpendicular NW-SE orientation (Fig. 7). The major extensional faults are predominantly basinward-dipping and detach into the salt, with small throws on associated antithetic faults (Fig. 5). Many salt-detached faults are listric and have an arcuate geometry in plan-view (Figs 5 and 7). Where landward-dipping counter-regional faults do form they lead to the development of supra-salt anticlines (e.g. Fig. 5). Growth strata in the hangingwalls of the faults indicate that fault activity initiated in the Pliocene, after the deposition of a thin pre-kinematic layer (Allen et al., 2016; Elfassi et al., 2019).

A series of closely-spaced, supra-salt buckle folds are located down-dip of the extensional structures in the northern part of the study area (Fig. 7). The fold axes are NE-oriented (sub-parallel to the salt rollers in the extensional domain) and they have a peak-to-peak wavelength of c. 1.2 km. The overburden in the southern part of the dataset, however, remains largely undeformed and shows little evidence of supra-salt contraction.

4.3 Intrasalt Stratigraphy

The Messinian evaporite sequence in the Levantine Basin comprises characteristically chaotic, low-amplitude, halite-dominated units interbedded with bright, semi-continuous reflections (Fig. 5). These reflective packages are widely documented across the eastern Mediterranean, and indicate lithological heterogeneity within the evaporite sequence (Netzeband et al., 2006; Lofi et al., 2011;

Gvirtzman et al., 2013; Feng et al., 2016; Camerlenghi et al., 2019). Herein, we use the Messinian stratigraphic nomenclature defined by Feng et al. (2017), where the six intrasalt units are termed (from oldest/deepest to youngest/shallowest): ME1, ME2, MC1, ME3, MC2 and ME4 (Fig. 9). ME is used to refer to the chaotic (halite-dominated) units whereas MC refers to the reflective units. These correspond to Units 1 to 6 in Gvirtzman et al. (2013), and ME-I to ME-VI in Netzeband et al. (2006).

The reflective units have been variably interpreted as interbeds of evaporites (gypsum and anhydrite) and clastics (e.g. Netzeband et al., 2006; Cartwright and Jackson, 2008; Feng et al., 2016). The hazard and high drilling cost associated with the recovering of cores within the MSC has resulted in a lack of hard data to constrain the intrasalt stratigraphy. Netzeband et al. (2006) interpret the evaporitic units to reflect depositional cycles caused by temporal changes in brine salinity driven by variations in sea level. They suggest that this led to interbedding of the thick, ductile halite with more rigid evaporites and/or clastic sediments. Feng et al. (2017) and Gvirtzman et al. (2017) use petrophysical data from boreholes to interpret a succession of thin, clay-rich, clastic interbeds. Feng et al. (2017) also use an amplitude extraction on the intrasalt horizons to interpret a possible network of basin floor fans, supporting a clastic mode of deposition. Industrial activity targeting new hydrocarbon prospects has provided new data, and Meilijson et al. (2019) recently published the first publicly available report using borehole cuttings to analyse the lithologies of the units at two localities in the Levantine Basin, offshore Israel. They confirm that the reflective units comprise a high proportion of clay material, with layers of argillaceous diatomites found within MC1 and at top-ME1, and mixed clastic-evaporitic interbeds with anhydrites dominating MC2. We are therefore confident that the reflective units imaged in the present dataset comprise clastic (mostly clay-rich) interbeds, but the detailed evaporitic heterogeneity and lateral facies continuity remain largely unconstrained. Local factors, such as proximity to clastic supply and topography of the basin, are likely to result in significant differences between the Messinian stratigraphic succession in different parts of the Mediterranean. Exposures of Messinian deposits in marginal basins of the Mediterranean (e.g. in the Realmonte Salt Mine, Sicily) and analogous evaporite sequences in other basins (e.g. in the Wieliczka Salt Mine, Poland), show that intrasalt heterogeneity occurs on a range of scales, from mm-scale crystalline impurities up to the decametre bedding scale (Fig. 1).

The total thickness of the Messinian evaporitic sequence increases seaward toward the centre of the basin and pinches out updip on the Levant margin (Fig. 10a). Thickness maps of the halite-dominated units ME1, ME2 and ME3 show relatively little variation across the contractional domain (Fig. 10b-d). The oldest unit ME1 does, however, thicken across the sub-salt normal faults (Fig. 9; Fig. 10b). The fact that there appears to be little intrasalt thickness variation across the dataset indicates that contractional (vertical) thickening of the layers has been broadly uniform across the study area.

MC1 consists of three semi-continuous, high-amplitude, sub-parallel reflections that can be traced across most of the basin (Figs 9 and 10e). The thickness map for MC1 shows a broadly uniform average thickness of 85 ms TWT (c. 170 m) across the contractional domain of dataset (Fig. 10d), with local thickness variations attributed to reverse faulting (e.g. Fig. 9). This unit has a very similar expression and thickness in the southern Levantine Basin, offshore Israel (Gvirtzman et al., 2013; Feng et al., 2016) and in the deep basin, offshore Lebanon (Kirkham et al., 2020).

In contrast, MC2 comprises between 4-6 discrete intrasalt reflections and does show some basinward thickening into the contractional domain, largely due to the angular truncation of intrasalt reflections against the top-salt in updip areas (Figs 9 and Fig. 10f). Where the full stratigraphy of the unit is preserved it reaches thicknesses of 180 ms TWT (c. 360 m). In comparison, MC2 is overall thicker to the south, offshore Israel, averaging 450 m (Feng et al., 2016). This may reflect lateral depositional variability, likely related to the large input of clastic material from the proximal Nile Delta in the southern Levantine Basin.

Both units MC1 and MC2, as well as the top-ME1 reflector, show some lateral variation in the amplitude and continuity of the reflections (Fig. 5). In some places they are very dim and the salt becomes seismically transparent, which may once again reflect lateral depositional variability in the thickness and composition of the units.

4.4 Intrasalt Structure and Strain

Intrasalt reflections are folded and faulted across the basin, even where they directly underlie extensional structures in the overburden (Fig. 5). Structure maps of the intrasalt reflectors show that the fold axes and thrust planes strike dominantly NNE-SSW (Fig. 11). The thrust faults are 2-5 km long and have an arcuate trace in plan view (Fig. 11). They are relatively closely spaced (mostly 1-2 km apart), forming segmented, en echelon arrays separated by unbreached or breached relay ramps. The thrust planes dip exclusively to the SE with hangingwall folds verging to the NW across the study area (Figs 5 and 9).

The strike of the faults and fold axes is consistent for all mapped horizons within the salt. While most intrasalt faults have small displacements (<70 ms or c. 300 m) and are confined to their discrete reflective units, some larger displacement faults (up to 160 ms or c. 670 m) connect MC1 and MC2 and cross-cut the intervening halite-dominated ME3 (Fig. 9). The intrasalt faults are fully confined to the salt, terminating at the top-salt, and do not extend up into the overburden. Finally, we observe that some structures in the overburden appear to be concordant with intrasalt structures (i.e.

overburden folds directly overlying intrasalt thrusts of the same length and orientation), but in other places intrasalt structures have no expression in the overlying overburden (Fig. 9).

The distribution of the seismically imaged intrasalt strain is highly heterogeneous, varying both vertically and laterally across the study area. First, strain on individual reflections can vary by significant amounts (up to 200%) laterally over relatively short length-scales (i.e. between profiles only 8 km apart). Overall strain increases southward, but with significant local variability within the area of interest (Fig. 12). For example, abrupt local increases in strain occur where intrasalt thrust duplexes are developed, accommodating a large amount of shortening over a relatively short distance, with strain reducing significantly away from the structure (Fig. 13).

The cause of such extreme strain localisation is unclear. One possible explanation is that it relates to relief on the base-salt surface which causes salt flow lines to converge and thus promotes local contraction (Dooley et al., 2017). The magnitude of relief on the base-salt surface appears relatively small in the presented two-way-time data, but since the reflective packages are acoustically slower than the salt (Reiche et al., 2014; Feng et al., 2016), a depth-converted section may show the true relief to be significantly greater. This highlights the importance of lithologically-controlled variations in intrasalt velocity when building velocity models and undertaking depth conversion. A uniform velocity model applied to the entire salt sheet would not account for the lateral velocity variations due to intrasalt structural complexity and would therefore inaccurately distort the base-salt structure map. Conversely, other base-salt anticlines mapped in this study are not associated with such extreme strain localisation or development of intrasalt duplex structures. An alternative interpretation is that strain localisation may reflect depositionally-controlled lateral facies changes and associated lateral variations in the bulk strength of the deforming salt sheet. If the salt was locally weaker due to, for example, an increased proportion of halite and/or thinner clastic units, this would make it more prone to accommodate any applied stress, serving to localise strain.

The intrasalt strain also appears to vary vertically, as well as laterally, within the deforming salt sheet (Fig. 9). The averaged vertical strain profile shows that the top-ME1 reflection near the base of the sheet exhibits the least strain, likely due to increased boundary drag and shear stress at the contact with the fixed base-salt surface. Maximum strains occur in the centre of the salt sheet at the base of MC1, with strain decreasing gradually toward the top of the salt sheet in MC2, and a sharp decrease at the erosional contact with the overlying clastic overburden (Fig. 9). In fluid mechanics, this resembles an asymmetric Poiseuille flow distribution (Fig. 3c). However, since strain is only measurable in the brittle units, cryptic strain within the ductile units may be even higher, as has been shown in some physical models (e.g. Fig. 14; Weijermars and Jackson, 2014). Strain remains very low in the overburden relative to the intrasalt units.

5 Salt Tectonics

In this section we review the observations described in detail above and pull these together to form an integrated salt tectonic framework for the Lebanese Levant margin. We interpret the implications of our observations in terms of gravity gliding, the interaction of salt flow with base-salt relief, the rheology of the evaporite sequence, and the multiphase evolution of salt deformation.

5.1 Gravity Gliding

The Levant passive margin can be divided into kinematically-linked salt tectonic domains of updip extension and downdip contraction, with the listric geometry of the detached supra-salt faults typical of thin-skinned tectonics on salt-influenced margins (Fig. 5) (Jackson and Hudec, 2017). Their orientation parallel to the margin and closely following the base-salt dip is indicative of a system dominated by gravity gliding (Jackson et al., 1994; Jackson and Hudec, 2017) (Figs 6 and 7). The dominant NE-SW structural trend of the supra-salt faults and buckle folds, as well as the basinward vergence and trend of the intrasalt faults and folds, indicates a dominant NW direction of transport. This differs significantly from the NE direction of transport indicated by the structural trend offshore Israel, c. 150 km to the south of the present study area (Cartwright et al., 2012). This is attributed to the proximity of the Nile Delta and the associated increased gravity spreading component in the southern Levantine Basin, the influence of which decrease northwards along the Levant margin (Allen et al, 2016).

The supra-salt buckle folds are present only in the northern part of the study area, whereas in the southern part of the study area there is very little overburden contraction despite significant extension updip. This can be attributed to the proximity of the folds to the Latakia Ridge, which acts as a buttress to basinward salt flow and thus confines the formation of contractional structures to a relatively narrow belt. The overburden in the southern part of the study area may therefore appear weakly deformed because the contraction is more diffuse and taken up over a greater area, or because the translational zone is much wider, with the buckle folds located further downdip of the available dataset.

5.2 Influence of Base-Salt Relief

The flow of salt over relief on the base-salt surface has affected the structural evolution of the salt and overburden in two notable ways. First, the NE-trending base-salt anticlines have caused the development of several ramp syncline basins in the overburden, recognised by their landward-dipping growth strata and onlap surfaces adjacent to the sub-salt anticlines (Fig. 5) (Jackson and Hudec, 2005;

Pichel et al., 2018). Ramp-syncline basins record simple basinward (horizontal) translation and are not associated with any contractional (e.g. folds or thrusts) or extensional (e.g. normal faults) structures in the overburden, therefore there is no apparent effect of changes in salt flux across the base-salt anticlines (cf. Dooley et al., 2017; Pichel et al., 2018).

Second, the expression of the underlying NW-SE-striking sub-salt faults (Fig. 6) can be seen in the thickness map of ME1 (Fig. 10b) and in the structure map of the top-ME1 reflector. Thickening across the base-salt faults likely reflects the syn-depositional infilling of residual topography on the base-salt surface, suggesting the faults were active up to, or during, the deposition of ME1 in the early stage of the Messinian Salinity Crisis. This supports the interpretation made by Reiche et al. (2014) that these faults may have contributed to the development of small fault-propagation folds that deformed the top-ME1 reflection. Reiche et al. (2014) also interpret shallower intrasalt structures in units MC1 and MC2 on 2D seismic lines, and suggest that these early fault-propagation folds may have accommodated and focused later tectonic shortening. However, the younger evaporitic units mapped within our 3D survey do not appear to show any expression of these subsalt faults, nor any related thickness changes, and the orientation of the intrasalt contractional structures is different to that of the sub-salt faults. We therefore conclude that fault activity had ceased during the deposition of ME2, and that the residual base-salt relief does not appear to have had any significant effect on salt flow due to the orientation of the faults parallel to the direction of salt flow, as well as their small throw (c. 70 m) relative to the large evaporite thickness (up to 2 km).

5.3 Salt Rheology

Lithological heterogeneity gives rise to rheological heterogeneity, since the different lithologies have different mechanical properties (e.g. Albertz and Ings, 2012; Raith et al., 2016; Rowan et al., 2019). This controls the way in which the intrasalt units respond to applied stresses and accommodate strain. The reflective units MC1 and MC2 demonstrate dominantly brittle behaviour during deformation, accommodating most of the contraction with slip on reverse faults (Figs 9 and 11). This contrasts with the intervening halite-dominated units, which deform in a bulk ductile manner, accommodating strain principally by viscous flow and thickening. No brittle deformation of these units is visible in the seismic data.

Our observations are consistent with those of Netzeband et al. (2006) and Gvirtzman et al. (2013), in that MC1 and MC2 appear to be largely independently faulted and folded, with the ductile halite-dominated layers acting as intra-Messinian detachment levels within the deforming sequence. Netzeband et al. (2006) assert that the lack of coupling between the units is evidence for syn-depositional deformation. However, mechanical decoupling of the brittle layers via the intervening ductile layers could also account for this disharmonic deformation (Cartwright et al., 2012; Allen et al.,

2016). Furthermore, we observe that some of the larger reverse faults appear to cross-cut the halite-dominated ME3 unit to vertically link faults in MC1 and MC2. We therefore suggest that small, thrust-related vertical displacements may be absorbed by ductile deformation of the ME3 halite unit, allowing the development of discrete, layer-bound structures within MC1 and MC2, whereas larger vertical displacements that impose larger vertical stresses (e.g. due to hangingwall uplift) are able to propagate through the halite to link otherwise discrete structures in MC1 and MC2.

5.4 Multiphase Salt Flow

The gently folded Pliocene overburden is demonstrably much less deformed than the underlying intrasalt units (Fig. 9). This phenomenon has been variably interpreted as a result of multiphase salt flow (Netzeband et al., 2006; Gvirtzman et al., 2013; Feng et al., 2017; Kartveit et al. 2018), or mechanical decoupling of the salt and overburden, accommodated by shear drag at the contact (i.e. top-salt) (Cartwright et al., 2012).

The contact between the salt and overburden (i.e. top-salt) is also an erosional unconformity (Fig. 9). The observed thickness variations across MC2 are largely attributed to erosion of the unit in the updip domain, as indicated by the truncated intrasalt reflections against the top-salt surface (Figs 5 and 10f). This means that seaward salt flow, and erosion of the crests of developing structures, initiated prior to the deposition of the present-day overburden. This is consistent with interpretations by Gvirtzman et al. (2017) offshore Israel, and more recently by Kirkham et al. (2020) offshore Lebanon, who postulate dissolution of structural highs due to impingement of the halocline in a stratified water column. This truncation is conclusive evidence that there have been at least two discrete phases of salt flow on the Levant margin, first pre- and then post-overburden deposition (cf. Netzeband et al., 2006; Gvirtzman et al., 2013; Gvirtzman et al., 2017; Feng et al. 2017; Kartveit et al. 2018). Gvirtzman et al. (2013) also use thickness changes within salt layers and intrasalt onlaps as evidence of syn-depositional flow but no such evidence is documented in the present dataset. We note that even post-depositional deformation can lead to thickness changes within the mobile, halite-dominated salt layers, and that geophysical artefacts may resemble apparent onlaps (Albertz and Ings, 2012; Allen et al., 2016).

The multiphase flow model also explains the observed differences between the type and distribution of structures in the intrasalt units compared to the overburden. If both were deformed together we would expect more concordance between overburden and intrasalt structures (i.e. intrasalt faults with large throws associated with uplift in the overlying supra-salt strata).

Shallow growth strata in the overburden and relief on the seabed indicate that active salt tectonics continue to influence the structural evolution of the Levant margin to the present day. Whereas some salt-related structures appear to show recent growth, as indicated by their expression in the overlying overburden and recent growth strata, others have become inactive and show no evidence of activity post-overburden burial (e.g. Fig. 9).

6 Discussion

The Poiseuille strain profile derived from seismic data in this study is consistent with strain measurements offshore Israel (Cartwright et al., 2012), although the net direction of tectonic transport and salt flow is different (i.e. NW as opposed to NE). However, recent studies by Cartwright et al. (2018) and Kirkham et al. (2019), which utilise a series of deformed fluid escape pipes and related pockmarks within the post-salt overburden, suggest that the salt layer deformed predominantly by Couette (Fig. 3b) rather than Poiseuille flow (Fig. 3a). The passively deformed fluid escape pipes are interpreted as direct kinematic indicators and show the greatest amount of strain at the top of the salt, decreasing exponentially toward its base. Here we discuss two ways in which these seemingly contrasting flow patterns (Poiseuille vs. Couette) may be reconciled.

6.1 Subseismic Strain

First, we discuss the way in which strain is accommodated by the different brittle units, decoupled by the intervening halite-dominated, ductile layers. Seismic data show differences between units MC1 and MC2 in terms of the number and spacing of intrasalt reflections; however, seismic data alone does not allow us to determine the detailed lithological heterogeneity. We know that lithological heterogeneity is common in evaporitic sequences (Fig. 1) and that this heterogeneity occurs at a range of scales; seismic data images only the very upper end of this scale (i.e. >10 m). The available well data also suggest lithological differences between MC1 and MC2, and that they comprise slightly different thicknesses of clastic interbeds (Meilijson et al., 2019).

Constraining the intrasalt lithological heterogeneity of the Messinian salt is important, given it controls how the unit deforms and what we can image seismically. Deformed, heterogeneous evaporites exposed in the Wieliczka Salt Mine show that strain is accommodated differently between different units (Fig. 15; Burliga et al., 2018). A m-scale thrusted and recumbently folded structure exposed in the wall of the mine contains within it several smaller broken units which are too small to be imaged by seismic reflection data. This means we would be unable to identify, map, and measure the associated strain with seismic data. Although the Serravallian evaporites exposed in the mine are older and more deformed than the Messinian, it is plausible that the different units within the Messinian sequence, with different rheological behaviours, would also accommodate strain differently.

If the upper reflective unit MC2 accommodates more sub-seismic deformation (i.e., short-wavelength folds and/or low-displacement faults), the unit may falsely appear to be more weakly strained in seismic reflection data than it actually is (Fig. 16). It is also noted that even though the reflective layers appear to deform in a dominantly brittle manner, some strain may also be accommodated by cryptic

compaction and/or bed thickening. Again, a seismic-based strain analysis would not detect this and we may therefore be missing a significant and as yet unquantified percentage of the actual strain (Fig 16). This could account for the discrepancy between the lower strain calculated for MC2 in the seismic data, versus the higher strain indicated by the deformed pipes.

This leads us to speculate as to the composition of MC2, such that it accommodates more strain by the formation of sub-seismic structures, and therefore appears at the seismic-scale to be more weakly deformed than MC1. Even small differences in the lithological stratigraphy of the units may have a significant effect on how they respond to applied stress. The thicknesses of the brittle interbeds may play an important role here as bed thickness is a first-order control on how strain is accommodated. For example, thicker, stronger beds develop folds with a greater dominant wavelength than thinner, weaker beds (Fossen, 2016). The brittle intrasalt layers are too thin to separately resolve their top and base with seismic data; the 'soft kick' of the top of the layer is immediately followed by the 'hard kick' of the base of the layer, with the resulting superposition generating a single wavelet (Brown, 2011). There may therefore be unresolved differences in bed thicknesses between MC1 and MC2. Since fold amplitude is proportional to bed thickness, if MC2 were composed of thinner beds it is possible that more of the strain would be accommodated by short-wavelength, small-amplitude, sub-seismic structures than MC1, within which thicker beds promote the development of large-amplitude, seismically resolvable structures (Fig. 16). Discordant folding of beds with different thicknesses is evident in onshore exposures of Messinian evaporites in marginal basins, such as those in Sicily (Butler et al., 2015).

The way in which the reflective units accommodate strain is not only determined by the lithology and thickness of individual beds within the sequence, but also by the properties of the sequence as a whole. For example, physical models show that the rheology of an individual sand layer is sensitive to the thickness of silicone within which it is encased (Fig. 17). In a closed, gravity-driven system, sand layers encased in thick silicone accommodated horizontal shortening by large-amplitude ductile folding, whereas sand layers encased in thin silicone accommodated strain on discrete brittle thrusts (Fig. 17). Therefore, perhaps it is the overall ratio of brittle-ductile materials in the sequence that exerts a primary control on the resulting deformation.

Physical models using silicone as a salt analogue have previously shown that higher brittle-ductile strength ratios result in greater localisation of strain whereas more ductile sequences result in more distributed strain. Davy et al. (1995) define the brittle-ductile parameter (Γ), which controls the large-scale localization of deformation, and associated fault patterns (both density and fault length distribution). Schueller and Davy (2008) use physical models to show that strain localization occurs

481 when Γ = >0.5. For smaller Γ, the large-scale deformation, although heterogeneous, never localizes. Γ
482 = 0.5 can be considered as a rheological transition between ductile-like macroscale rheology and
483 brittle-like one. In order for seismic-scale thrusts to develop, strain must localise on individual
484 structures such that they accumulate a critical amount of displacement that can be seismically
485 resolved. We could therefore speculate that MC2 has a smaller Γ than MC1, which means that it is
486 more prone to accommodating strain on distributed, sub-seismic scale structures, as opposed to the
487 larger, discrete thrusts developed in the middle unit (Fig. 16).

488 6.2 Spatial and Temporal Variability in Salt Flow

489 An alternative way to explain the apparent discrepancy between flow profiles is that the salt layer was
490 subject to both Poiseuille and Couette flow, but that the relative contribution of each (and related
491 deformation) varied through time. On geological timescales, salt deformation can be approximated as
492 a viscoplastic fluid that flows in response to applied stresses, from areas of high pressure to low
493 pressure to reach an equilibrium state. Viscoplastic materials are defined by the presence of a yield
494 strength, under which strain increases linearly with stress and beyond which the material deforms at
495 constant stress. Materials that yield to applied stresses by continuous deformation are known as
496 ductile materials, as opposed to brittle materials which are characterized by the fact that rupture
497 occurs without any noticeable prior change in shape. If we treat the behaviour of the salt unit as
498 viscoplastic and the brittle intrasalt layers act as passive strain gauges, the salt will exhibit a Poiseuille
499 flow profile when responding to a pressure gradient such as a differential load, and a Couette profile
500 when the flow is drag-induced by a translating overburden.

501 In nature, seismic data image finite structural style but this may not be representative of the present
502 day stress state within the deforming sequence. Physical analogue models and numerical finite
503 element models have generated both Poiseuille (e.g. Cartwright et al., 2012; Gradmann and
504 Beaumont, 2012) and Couette flow (e.g. Brun and Mauduit, 2009; Schultz-Ela and Walsh, 2002),
505 demonstrating that salt flow is highly sensitive to the applied boundary conditions, i.e. the relative
506 contribution of gravity gliding vs. gravity spreading. It is therefore probable that the dominant flow
507 regime varies through time and space depending on the stresses applied locally to the salt sheet.
508 When differential loading dominates, salt will deform via Poiseuille flow, and when overburden drag
509 dominates, the salt will deform via Couette flow. These are end-members of a spectrum, and in cases
510 where the salt sheet experiences both differential loading and overburden drag, the resulting flow
511 profile will assume a hybrid form (i.e. asymmetric Poiseuille profile; Fig. 3c).

512 Based on the mechanical and kinematic arguments detailed above, two phases of deformation are
513 required to explain the present structure of the salt and its overburden (Fig. 18). The first phase is said

514 to have occurred syn-depositionally or shortly thereafter, during the Messinian, culminating in erosion
515 of structural highs, followed by a second, later phase in the Plio-Pleistocene, during which time thin-
516 skinned tectonics were reactivated, deforming both the salt and overburden (Netzeband et al., 2006;
517 Gvirtzman et al., 2013; Gvirtzman et al., 2017; Feng et al. 2017; Kartveit et al. 2018). During the early
518 phase of deformation, when there was little gravitational instability due to base-salt tilt, salt flow could
519 have been driven predominantly by a pressure gradient caused by differential loading (i.e., Poiseuille
520 flow) (Fig. 18b). These clastic wedges could then have been eroded in the same basinwide margin
521 uplift event that created the truncation of intrasalt reflections against the top-salt (Fig. 18c)
522 (Gvirtzman et al., 2017; Kirkham et al., 2020). Later, as basin subsidence resumed and a clastic
523 overburden was deposited above the salt, additional loading, combined with wholesale tilting of the
524 margin, could have caused a change to drag-induced (i.e., Couette) flow (Fig. 18e). This is consistent
525 with the model proposed by Cartwright et al. (2018) showing that the first fluid escape pipe formed
526 when some overburden (c. 250 m) had already been deposited. This means that the strain recorded
527 by the deformation of the intrasalt layers is the total flow (i.e., Poiseuille + Couette) experienced by
528 the salt (Fig. 19), whereas the strain recorded by the pipes reflects only the later Couette phase of
529 flow.

530 ## 6.3 Implications

531 We have shown that planning well paths to account for the present stress state within thick salt bodies
532 must consider the structural evolution of the salt and overburden, since strain profiles derived from
533 seismic data may be misleading. Complex rheological sequences mean that stress and strain are not
534 proportional, and that strain may not be accommodated uniformly within the deforming salt body.
535 Furthermore, temporal and spatial variability in the dominant flow regime could mean that the
536 cumulative strain distribution may not be representative of the present intrasalt stress state. It is
537 therefore important to develop an integrated understanding of the regional and local forces acting
538 upon the salt sheet, and driving deformation in the system, in order to predict the present stress state.
539 On the Lebanese Levant margin the salt in now undergoing a drag-induced Couette flow, and as such
540 a deviated drilling trajectory would be required to minimise shear stress on the borehole (Fig. 20;
541 Weijermars et al., 2014).
542
543 The heterogeneous distribution of strain within the deforming salt body also means that we must
544 account for intrasalt heterogeneity when building velocity models to accurately seismically image and
545 depth convert sub-salt structures. The presence of interbeds with relatively slow seismic velocities will
546 disrupt travel times, and as such the travel times will be sensitive to the geometry and distribution of
547 intrasalt structures, particularly where large stacked duplex structures occur (e.g. Fig. 13). We
548 therefore conclude that intrasalt structure and strain partitioning is an important consideration for
549 successful petroleum exploration and production, with implications for accurate velocity modelling
550 and efficient drilling through thick salt.

Conclusions

- Gravitationally-driven salt tectonics have dominated the Levant passive margin since the Messinian, with a dominant NW direction of transport
- Salt flow is locally restricted around the Latakia Ridge leading to more intense supra-salt deformation
- Reflective units within Messinian salt deform in a brittle manner and allow us to measure the relative seismic-scale intrasalt strain distribution
- The lateral seismic strain distribution is irregular, with locally high strains that reflect locally developed thrust duplexes
- Vertical strain profiles derived from seismic reflection data may not represent true flow profiles due to limitations in seismic resolution and differences in the way in which strain is accommodated between units with different rheologies
- The dominant flow regime (Poiseuille vs. Couette) may vary through time and space, predominantly due to changes in the relative contribution of differential loading (i.e. gravity spreading) and margin tilting (i.e. gravity gliding)

Acknowledgements

The authors wish to gratefully acknowledge Ramadan Ghalayini and the Lebanese Petroleum Authority for the provision of data, without which this project would not be possible.

References

Aal, A.A., El Barkooky, A., Gerrits, M., Meyer, H., Schwander, M. and Zaki, H., 2000. Tectonic evolution of the Eastern Mediterranean Basin and its significance for hydrocarbon prospectivity in the ultradeepwater of the Nile Delta. The Leading Edge, 19(10), pp.1086-1102.

Albertz, M. and Ings, S.J., 2012. Some consequences of mechanical stratification in basin-scale numerical models of passive-margin salt tectonics. Geological Society, London, Special Publications, 363(1), pp.303-330.

Allen, H., C.A.-L. Jackson and A.J. Fraser, 2016, Gravity-driven deformation of a youthful saline giant: the interplay between gliding and spreading in the Messinian basins of the Eastern Mediterranean: Petroleum Geoscience, v. 22, p. 340-356.

Balk, R. 1949. Structure of Grand Saline salt dome. AAPG Bulletin, 33, 1791–1829.

Ben-Avraham, Z., 1978. The structure and tectonic setting of the Levant continental margin, eastern Mediterranean. Tectonophysics, 46(3-4), pp.313-331.

Bertoni, C. and Cartwright, J.A., 2006. Controls on the basinwide architecture of late Miocene (Messinian) evaporites on the Levant margin (Eastern Mediterranean). Sedimentary Geology, 188, pp.93-114.

Bertoni, C. and Cartwright, J.A., 2007. Major erosion at the end of the Messinian Salinity Crisis: evidence from the Levant Basin, Eastern Mediterranean. Basin Research, 19(1), pp.1-18.

Brown, A.R., 2011. Interpretation of three-dimensional seismic data. Society of Exploration Geophysicists and American Association of Petroleum Geologists.

Brun, J.P. and Mauduit, T.P.O., 2009. Salt rollers: Structure and kinematics from analogue modelling. Marine and Petroleum Geology, 26(2), pp.249-258.

Burberry, C.M., 2015. Spatial and temporal variation in penetrative strain during compression: Insights from analog models. Lithosphere, 7(6), pp.611-624.

Burliga, S., P. Krzywiec, K. Dąbroś, J. Przybyło, E. Włodarczyk, M. Źróbek and M. Słotwiński. 2018. Salt tectonics in front of the Outer Carpathian thrust wedge in the Wieliczka area (S Poland) and its exposure in the underground salt mine: Geology, Geophysics & Environment, v. 44, p. 71-90.

Butler, R.W., Maniscalco, R., Sturiale, G. and Grasso, M., 2015. Stratigraphic variations control deformation patterns in evaporite basins: Messinian examples, onshore and offshore Sicily (Italy). Journal of the Geological Society, 172(1), pp.113-124.

Butler, R.W.H. and Paton, D.A., 2010. Evaluating lateral compaction in deepwater fold and thrust belts: How much are we missing from “nature’s sandbox”. GSA Today, 20(3), pp.4-10.

Camerlenghi, A., Del Ben, A., Hübscher, C., Forlin, E., Geletti, R., Brancatelli, G., Micallef, A., Saule, M. and Facchin, L., 2019. Seismic markers of the Messinian salinity crisis in the deep Ionian Basin. Basin Research.

Cartwright, J.A. and M.P.A. Jackson, 2008, Initiation of gravitational collapse of an evaporite basin margin: The Messinian saline giant, Levant Basin, eastern Mediterranean. Geological Society of America Bulletin, 120(3-4), pp.399-413.

607 Cartwright, J.A., M.P.A. Jackson, T.P. Dooley and S. Higgins, 2012, Strain partitioning in gravity-driven
608 shortening of a thick, multilayered evaporite sequence, in G.I. Alsop, S.G. Archer, A.J. Hartley, N.T.
609 Grant and R. Hodgkinson, eds., Salt Tectonics, Sediments and Prospectivity: GSL Special Publication
610 363, p. 449-470.

611 Cartwright, J., C. Kirkham, C. Bertoni, N. Hodgson and K. Rodriguez, 2018, Direct calibration of salt
612 sheet kinematics during gravity-driven deformation: Geology, v. 46, p. 623-626.

613 Coleman, A.J., Jackson, C.A-L. and Duffy, O.B., 2017. Balancing sub-and supra-salt strain in salt-
614 influenced rifts: Implications for extension estimates. Journal of Structural Geology, 102, pp.208-225.

615 Dooley, T.P., Hudec, M.R., Carruthers, D., Jackson, M.P.A. and Luo, G., 2017. The effects of base-salt
616 relief on salt flow and suprasalt deformation patterns—Part 1: Flow across simple steps in the base
617 of salt. Interpretation, 5(1), pp.SD1-SD23.

618 dos Reis, A.T., Gorini, C. and Mauffret, A., 2005. Implications of salt–sediment interactions on the
619 architecture of the Gulf of Lions deep-water sedimentary systems—western Mediterranean Sea.
620 Marine and Petroleum Geology, 22(6-7), pp.713-746.

621 Elfassi, Y., Gvirtzman, Z., Katz, O. and Aharonov, E., 2019. Chronology of post-Messinian faulting
622 along the Levant continental margin and its implications for salt tectonics. Marine and Petroleum
623 Geology, 109, pp.574-588.

624 Esestime, P., A. Hewitt, and N. Hodgson, 2016, Zohr–A newborn carbonate play in the Levantine
625 Basin, East-Mediterranean: First Break, 34(2), 87-93.

626 Feng, Y.E., Steinberg, J. and Reshef, M., 2017. Intra-salt deformation: Implications for the evolution
627 of the Messinian evaporites in the Levant Basin, eastern Mediterranean. Marine and Petroleum
628 Geology, 88, pp.251-267.

629 Feng, Y. E., A. Yankelzon, J. Steinberg, and M. Reshef, 2016, Lithology and characteristics of the
630 Messinian evaporite sequence of the deep Levant Basin, eastern Mediterranean: Marine Geology,
631 376, 118-131.

632 Fiduk, J.C. and Rowan, M.G., 2012. Analysis of folding and deformation within layered evaporites in
633 Blocks BM-S-8 &-9, Santos Basin, Brazil. Geological Society, London, Special Publications, 363(1),
634 pp.471-487.

635 Fossen, H., 2016. Structural geology. Cambridge University Press.

636 Gautier, F., G. Clauzon, J.P. Suc, J. Cravatte and D. Violanti, 1994, Age and duration of the Messinian
637 salinity crisis: R. Acad. Sci., Paris (IIA) 318, p. 1103–1109.

638 Ghalayini, R., Daniel, J.M., Homberg, C., Nader, F.H. and Comstock, J.E., 2014. Impact of Cenozoic
639 strike-slip tectonics on the evolution of the northern Levant Basin (offshore Lebanon). Tectonics,
640 33(11), pp.2121-2142.

641 Ghalayini, R., Homberg, C., Daniel, J.M. and Nader, F.H., 2017. Growth of layer-bound normal faults
642 under a regional anisotropic stress field. Geological Society, London, Special Publications, 439(1),
643 pp.57-78.

644 Gradmann, S. and Beaumont, C., 2012. Coupled fluid flow and sediment deformation in margin-scale
645 salt-tectonic systems: 2. Layered sediment models and application to the northwestern Gulf of
646 Mexico. Tectonics, 31(4).

Gvirtzman, Z., M. Reshef, O. Buch-Leviatan and Z. Ben-Avraham, 2013, Intense salt deformation in the Levant Basin in the middle of the Messinian salinity crisis: Earth and Planetary Science Letters, 379, 108–119.

Gvirtzman, Z., Manzi, V., Calvo, R., Gavrieli, I., Gennari, R., Lugli, S., Reghizzi, M. and Roveri, M., 2017. Intra-Messinian truncation surface in the Levant Basin explained by subaqueous dissolution. Geology, 45(10), pp.915-918.

Hall, J., Calon, T.J., Aksu, A.E. and Meade, S.R., 2005. Structural evolution of the Latakia Ridge and Cyprus Basin at the front of the Cyprus Arc, eastern Mediterranean Sea. Marine Geology, 221(1-4), pp.261-297.

Hawie, N., Gorini, C., Deschamps, R., Nader, F.H., Montadert, L., Granjeon, D. and Baudin, F., 2013. Tectono-stratigraphic evolution of the northern Levant Basin (offshore Lebanon). Marine and Petroleum Geology, 48, 392-410.

Hodgson, N., 2012. The Miocene hydrocarbon play in southern Lebanon. First Break, 30(12).

Hoy, R. B., Foose,R.M.& O'Neill, B. J. 1962. Structure of Winnfield salt diapir. AAPG Bulletin, 46, 1444–1459.

Hudec, M.R. and Jackson, M.P., 2007. Terra infirma: Understanding salt tectonics. Earth-Science Reviews, 82(1-2), pp.1-28.

Jackson,M.P.A., Cornelius, R. R., Craig, C. H., Gansser, A., Stocklin,J.& Talbot, C. J. 1990. Salt Diapirs of the Great Kavir. Geological Society of America, Boulder, Memoir, 177.

Jackson, M. P. A. 1995. Retrospective salt tectonics. In: Jackson, M.P.A., Roberts,D. G.& Snelson,S. (eds) Salt Tectonics, A Global Perspective. American Association of Petroleum Geologists, Tulsa, Memoir, 65, 1–28.

Jackson, M.P. and Hudec, M.R., 2017. Salt tectonics: Principles and practice. Cambridge University Press.

Jackson, M.P.A., B.C. Vendeville and D.D. Schultz-Ela, 1994, Structural dynamics of salt systems: Annual Review of Earth and Planetary Sciences, 22(1), pp.93-117.

Jackson, C.A.L., Jackson, M.P., Hudec, M.R. and Rodriguez, C.R., 2015. Enigmatic structures within salt walls of the Santos Basin—Part 1: Geometry and kinematics from 3D seismic reflection and well data. Journal of Structural Geology, 75, pp.135-162.

Jackson, M.P. and Hudec, M.R., 2005. Stratigraphic record of translation down ramps in a passive-margin salt detachment. Journal of Structural Geology, 27(5), pp.889-911.

Kartveit, K.H., Omosanya, K.O., Johansen, S.E., Eruteya, O.E., Reshef, M. and Waldmann, N.D., 2018. Multiphase structural evolution and geodynamic implications of Messinian salt-related structures, levant basin, offshore Israel. Tectonics, 37(5), pp.1210-1230.

Kirkham, C., Cartwright, J., Bertoni, C., Rodriguez, K. and Hodgson, N., 2019. 3D kinematics of a thick salt layer during gravity-driven deformation. Marine and Petroleum Geology, 110, pp.434-449.

Kirkham, C., Bertoni, C., Cartwright, J., Lensky, N.G., Sirota, I., Rodriguez, K. and Hodgson, N., 2020. The demise of a 'salt giant'driven by uplift and thermal dissolution. Earth and Planetary Science Letters, 531, p.115933.

686 Kupfer, D. H. 1962. Structure of Morton salt company mine, Weeks Island salt dome. AAPG Bulletin,
687 46, 1460–1467.

688 Lofi, J., Déverchère, J., Gaullier, V., Gillet, H., Gorini, C., Guennoc, P., Loncke, L., Maillard, A., Sage, F.
689 and Thinon, I., 2011. Seismic atlas of the Messinian Salinity Crisis markers in the Mediterranean and
690 Black Seas (Vol. 179, pp. 1-72). Société Géologique de France.

691 Meilijson, A., Hilgen, F., Sepúlveda, J., Steinberg, J., Fairbank, V., Flecker, R., Waldmann, N.D.,
692 Spaulding, S.A., Bialik, O.M., Boudinot, F.G. and Illner, P., 2019. Chronology with a pinch of salt:
693 Integrated stratigraphy of Messinian evaporites in the deep Eastern Mediterranean reveals long-
694 lasting halite deposition during Atlantic connectivity. Earth-Science Reviews.

695 Miralles, L., Sans, M., Gali,S.& Santanach, P. 2001. 3-D rock salt fabrics in a shear zone (Su´ria
696 Anticline, South-Pyrenees). Journal of Structural Geology, 23, 675–691.

697 Nader, F.H., Inati, L., Ghalayini, R., Hawie, N. and Daher, S.B., 2018. Key geological characteristics of
698 the Saida-Tyr Platform along the eastern margin of the Levant Basin, offshore Lebanon: implications
699 for hydrocarbon exploration. Oil & Gas Science and Technology–Revue d'IFP Energies nouvelles, 73,
700 p.50.

701 Netzeband, G. L., C. P. Hübscher, & D. Gajewski, 2006, The Structural Evolution of the Messinian
702 Evaporites in the Levantine Basin: Marine Geology, 230(3–4), 249–73.

703 Pichel, L.M., Peel, F., Jackson, C.A. and Huuse, M., 2018. Geometry and kinematics of salt-detached
704 ramp syncline basins. Journal of Structural Geology, 115, pp.208-230.

705 Quirk, D.G., Schødt, N., Lassen, B., Ings, S.J., Hsu, D., Hirsch, K.K. and Von Nicolai, C., 2012. Salt
706 tectonics on passive margins: examples from Santos, Campos and Kwanza basins. Geological Society,
707 London, Special Publications, 363(1), pp.207-244.

708 Raith, A.F., Strozyk, F., Visser, J. and Urai, J.L., 2016. Evolution of rheologically heterogeneous salt
709 structures: a case study from the NE Netherlands. Solid Earth, 7(1), p.67.

710 Reiche, S., Hübscher, C. and Beitz, M., 2014. Fault-controlled evaporite deformation in the Levant
711 Basin, Eastern Mediterranean. Marine Geology, 354, pp.53-68.

712 Roveri, M., R. Flecker, W. Krijgsman, J. Lofi, S. Lugli, V. Manzi, F.J. Sierro, A. Bertini, A. Camerlenghi,
713 G. De Lange, R. Govers, F.J. Hilgen, C. Hübscher, P.T. Meijer, & M. Stoica, 2014, The Messinian
714 salinity crisis: Past and future of a great challenge for marine sciences: Marine Geology, 352, 25–58.

715 Rowan, M.G., Urai, J.L., Fiduk, J.C. and Kukla, P.A., 2019. Deformation of intrasalt competent layers in
716 different modes of salt tectonics. Solid Earth, 10(3), pp.987-1013.

717 Ryan, W.B.F., 2009, Decoding the Mediterranean salinity crisis: Sedimentology 56, 95–136.

718 Schleder, Z., Urai, J. L., Nollet,S.& Hilgers,C. 2008. Solution–precipitation creep and fluid flow in
719 halite: a case study from the Zechstein (Z1) rocksalt from Neuhof salt mine (Germany). Geologisches
720 Rundschau, 97, 1045–1056.

721 Schueller, S., and P. Davy, 2008, Gravity influenced brittle-ductile deformation and growth faulting in
722 the lithosphere during collision: Results from laboratory experiments, J. Geophys. Res., 113, B12404.

723 Schultz-Ela, D.D. and Walsh, P., 2002. Modeling of grabens extending above evaporites in
724 Canyonlands National Park, Utah. Journal of Structural Geology, 24(2), pp.247-275.

725 Steventon, M.J., Jackson, C.A.L., Hodgson, D.M. and Johnson, H.D., 2019. Strain analysis of a
726 seismically imaged mass-transport complex, offshore Uruguay. Basin Research, 31(3), pp.600-620.

727 Strozyk, F., Van Gent, H., Urai, J.L. and Kukla, P.A., 2012. 3D seismic study of complex intra-salt
728 deformation: An example from the Upper Permian Zechstein 3 stringer, western Dutch offshore.
729 Geological Society, London, Special Publications, 363(1), pp.489-501.

730 Talbot, C. J. 1998. Extrusions of Hormuz salt in Iran. In: Blundell,D.J.& Scott, A. C. (eds) Lyell, the Past
731 is the Key to the Present. Geological Society, London, Special Publications, 143, 315–334.

732 Van Gent, H., Urai, J.L. and De Keijzer, M., 2011. The internal geometry of salt structures–a first look
733 using 3D seismic data from the Zechstein of the Netherlands. Journal of Structural Geology, 33(3),
734 pp.292-311.

735 Weijermars, R. and M.P.A. Jackson, 2014, Predicting the depth of viscous stress peaks in moving salt
736 sheets: Conceptual framework and implications for drilling: AAPG Bull., v. 98, p. 911–945.

737 Zak, I. and Freund, R., 1980. Strain measurements in eastern marginal shear zone of Mount Sedom
738 salt diapir, Israel. AAPG Bulletin, 64(4), pp.568-581.

Figures

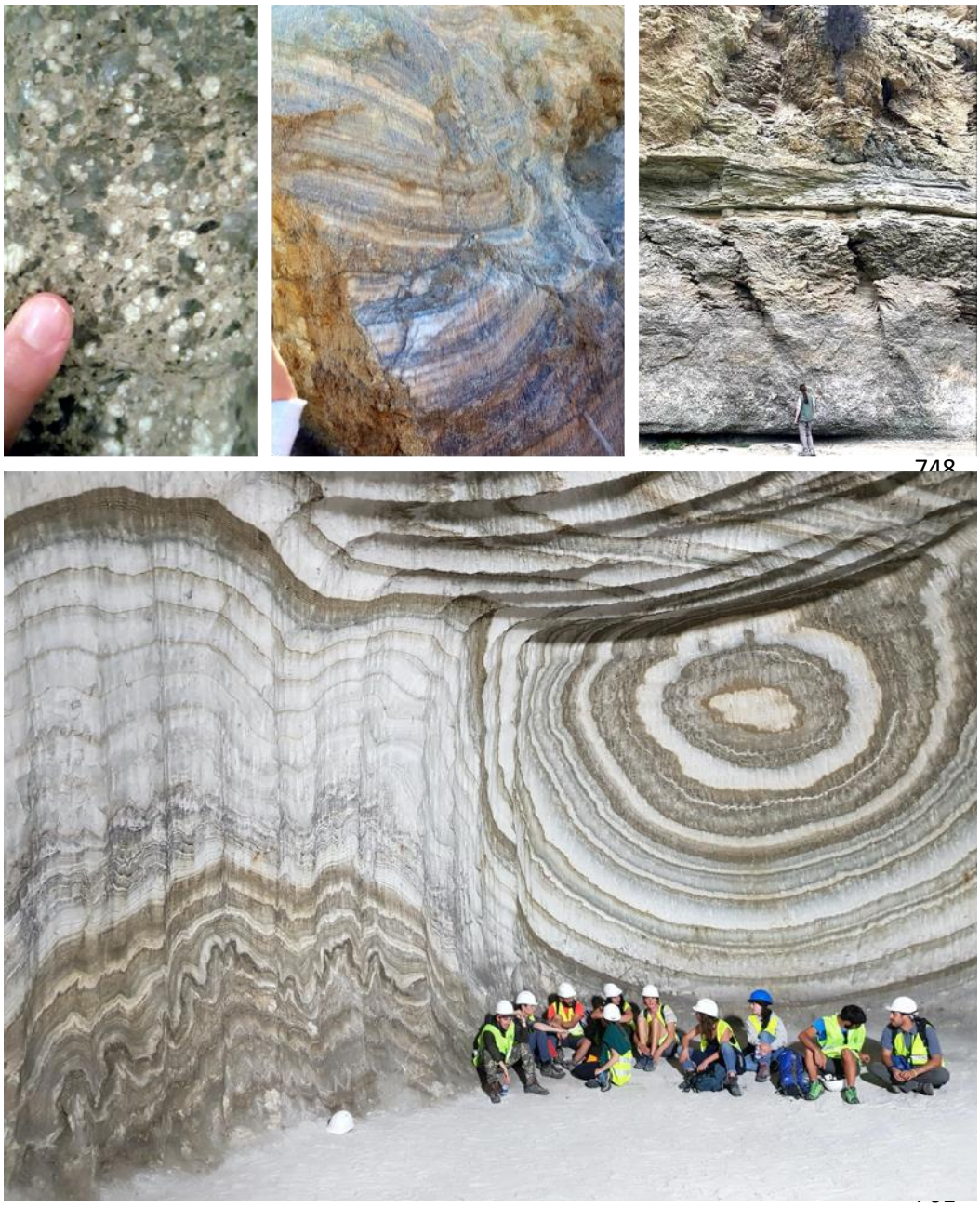

Figure 1 Compositional intrasalt heterogeneities on a range of scales: a) Coarse, angular crystals of halite and anhydrite in a clay-rich matrix from the Serravallian evaporite sequence exposed in the Wieliczka Salt Mine, situated close to Krakow in Poland; b) Interbedded layers of halite, gypsum and anhydrite from the Late Miocene-Pliocene evaporite sequence of the Mount Sodom diapir, Israel; c) Microbial gypsum trees and layered gypsum deposits in Sorbas, southern Spain; d) Deformed layers of Messinian age halite, gypsum, anhydrite ad clay layers exposed in the Realmonte salt mine, Sicily.

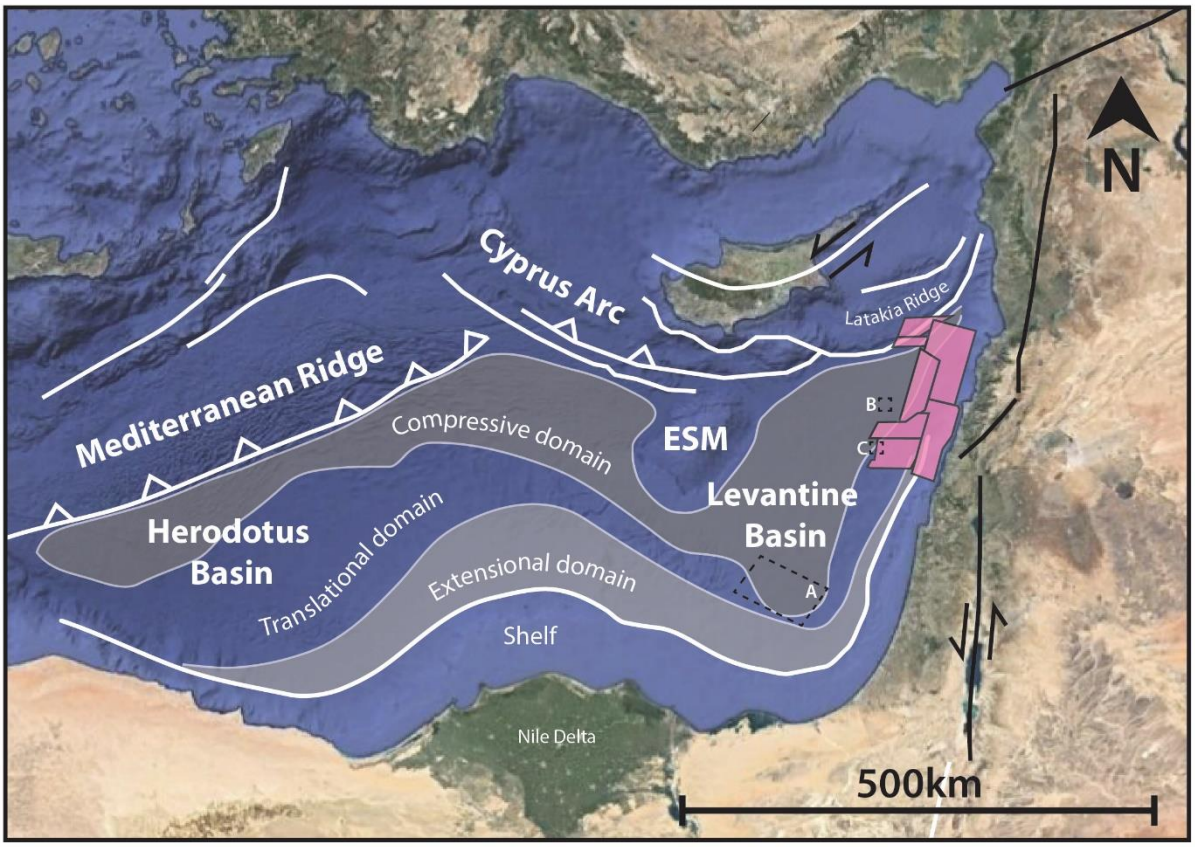

768 **Figure 2** Location of 3D seismic data used in this study (pink polygons), and regional context showing
769 distribution of key tectonic elements in the eastern Mediterranean (modified from Allen et al. 2016).
770 Boxes A, B and C indicate the locations of previous studies by Cartwright et al., (2012), Cartwright et
771 al., (2018) and Kirkham et al., (2019) respectively.

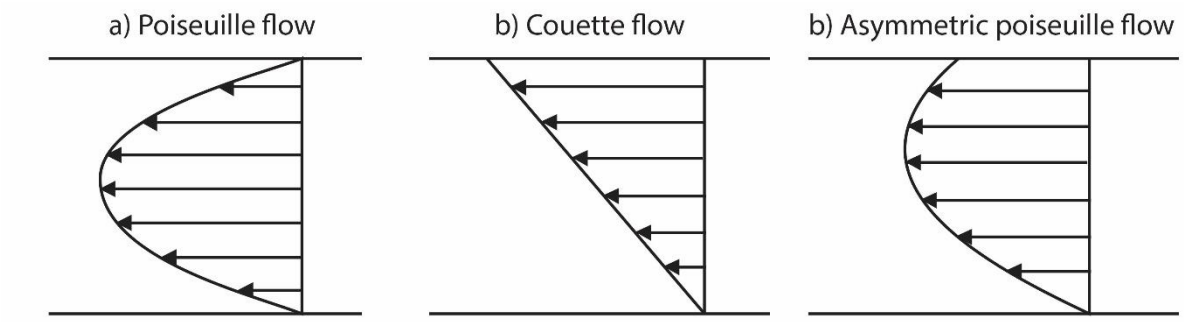

772 **Figure 3** Idealised flow profiles through a viscous salt sheet: (A) Poiseuille flow (pressure-induced), (B)
773 Couette flow (drag-induced), and (C) asymmetric Poiseuille flow (combination of pressure- and drag-
774 induced).

775

776

777

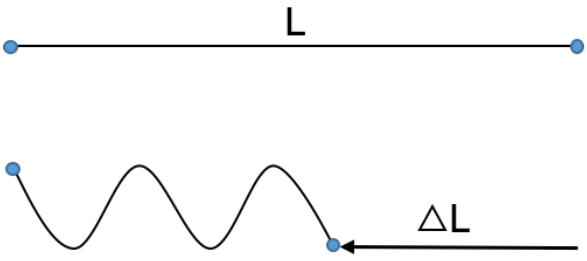

778

779

780

781

782

$$\varepsilon = \frac{\Delta L}{L}$$

783 **Figure 4** Calculation of strain using preservation of bed lengths during contraction (change in length
784 as a proportion of original bed length).

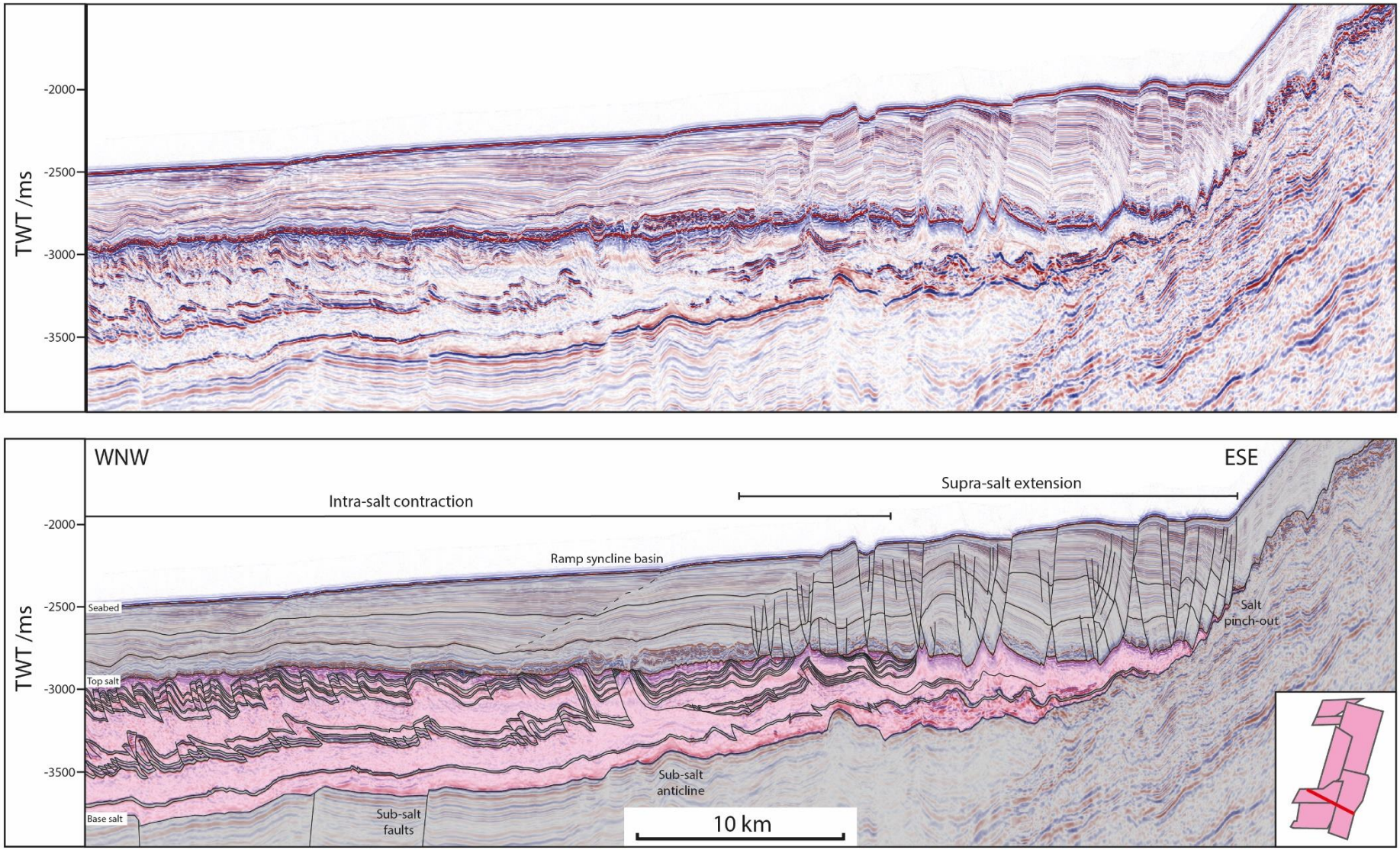

785 **Figure 5** Seismic section (upper) and interpretation (lower) showing updip supra-salt extension where salt pinches out, and deformed intrasalt reflections
786 truncating against top-salt. Location shown on inset map and Figures 6 and 7.

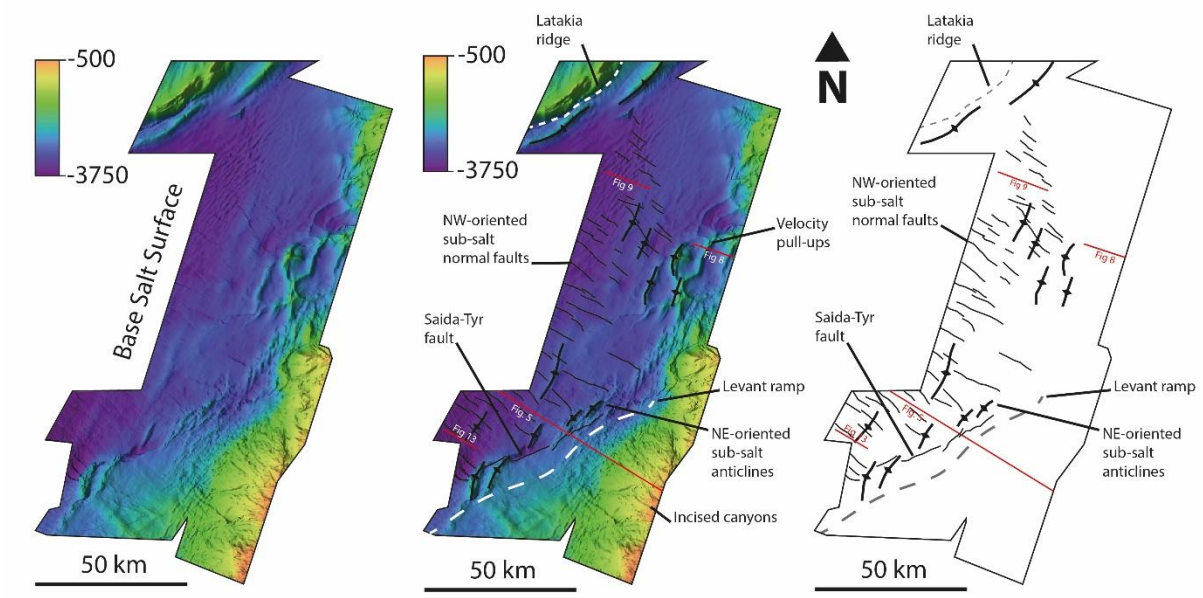

787 **Figure 6** Annotated structure map showing relief on the base-salt surface, in particular the
788 distribution of sub-salt anticlines and normal faults.

789

790

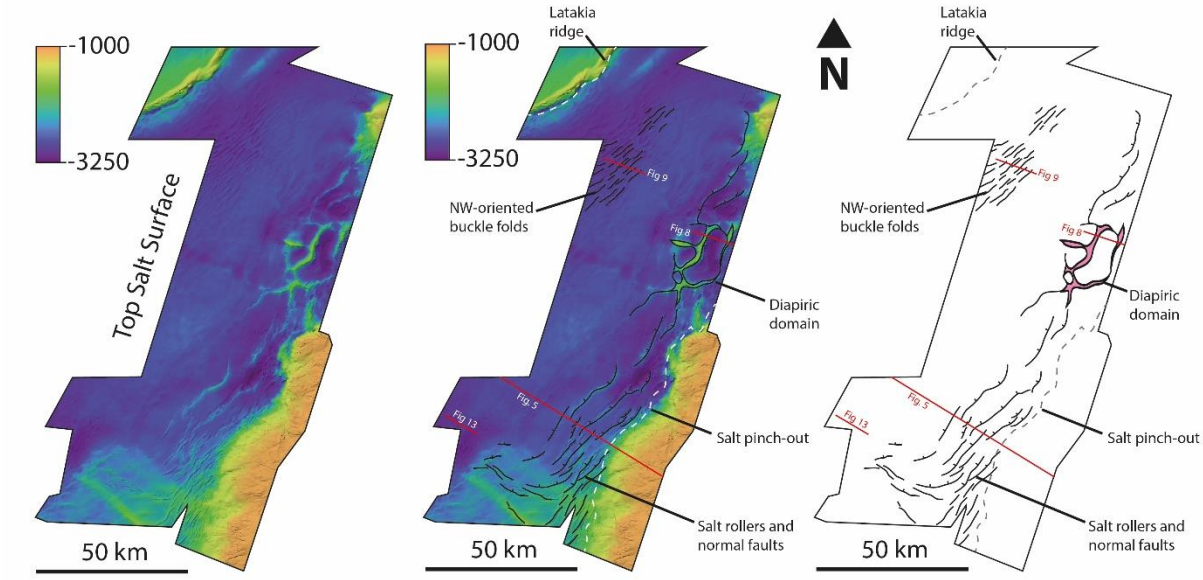

791 **Figure 7** Annotated structure map showing relief on the top-salt surface, in particular the
792 distribution of supra-salt normal faults, reactive diapirs and buckle folds.

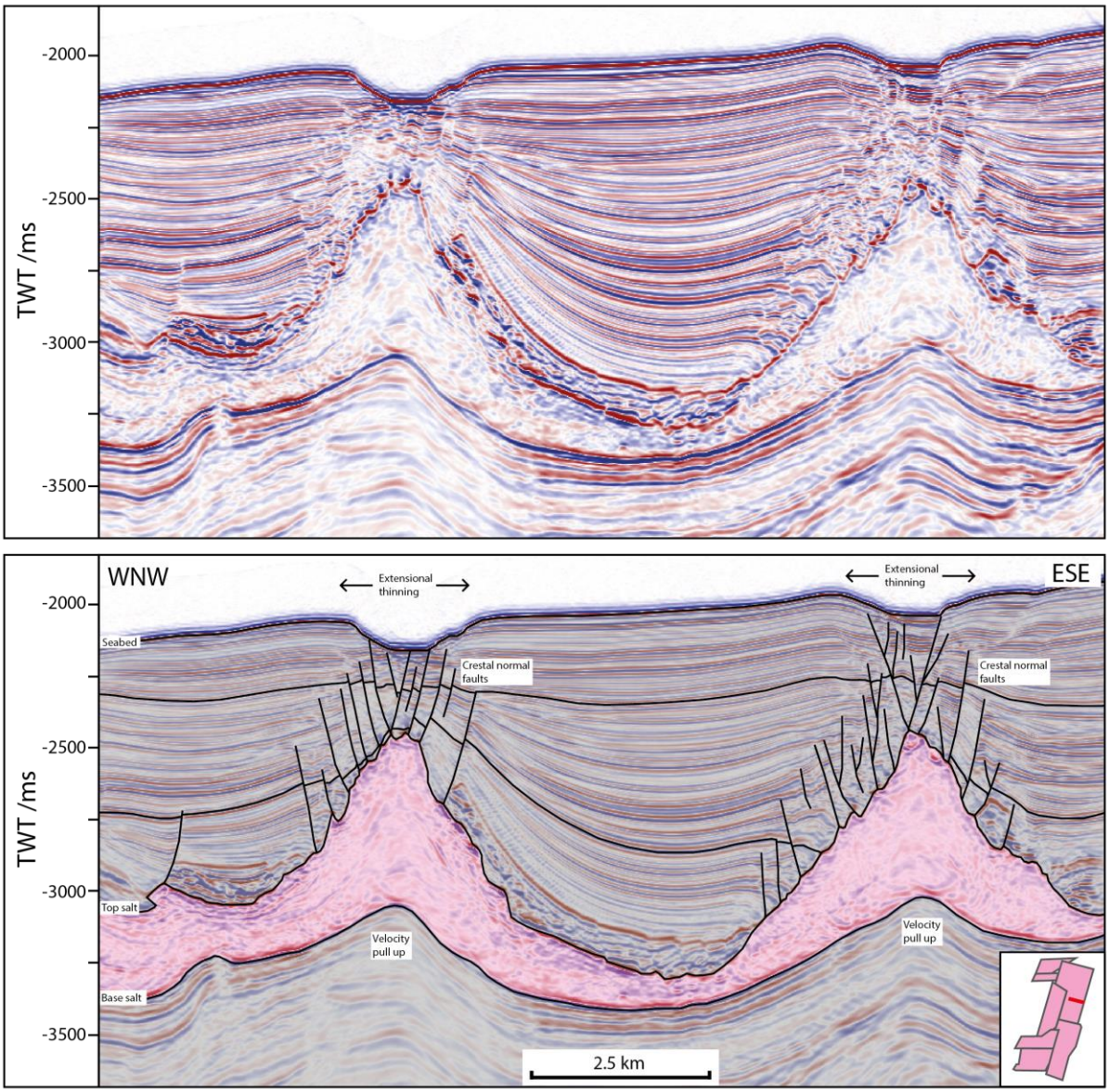

793 **Figure 8** Seismic section (upper) and interpretation (lower) showing mature reactive diapirs with
794 crestal normal faults corresponding to velocity pull-ups. Location shown on inset map and Figures 6
795 and 7.

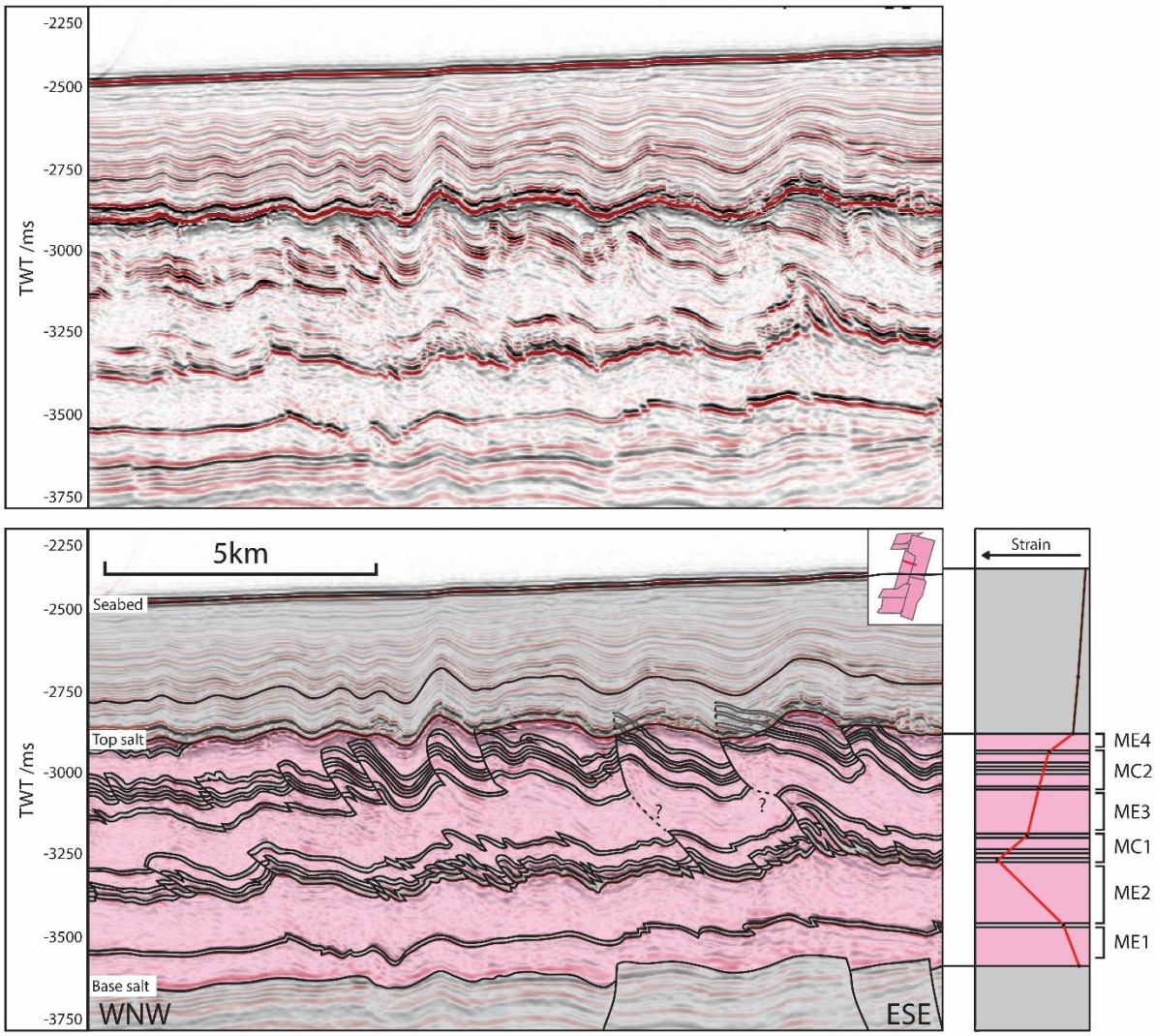

Figure 9 Seismic section (upper) and interpretation (lower) showing intrasalt stratigraphy and structure within the contractional domain. Vertical seismic strain profile calculated on brittlely deforming intrasalt reflectors (extrapolating upper reflectors to account for truncation at the top-salt) shows maximum strain in centre of the deforming salt sheet.

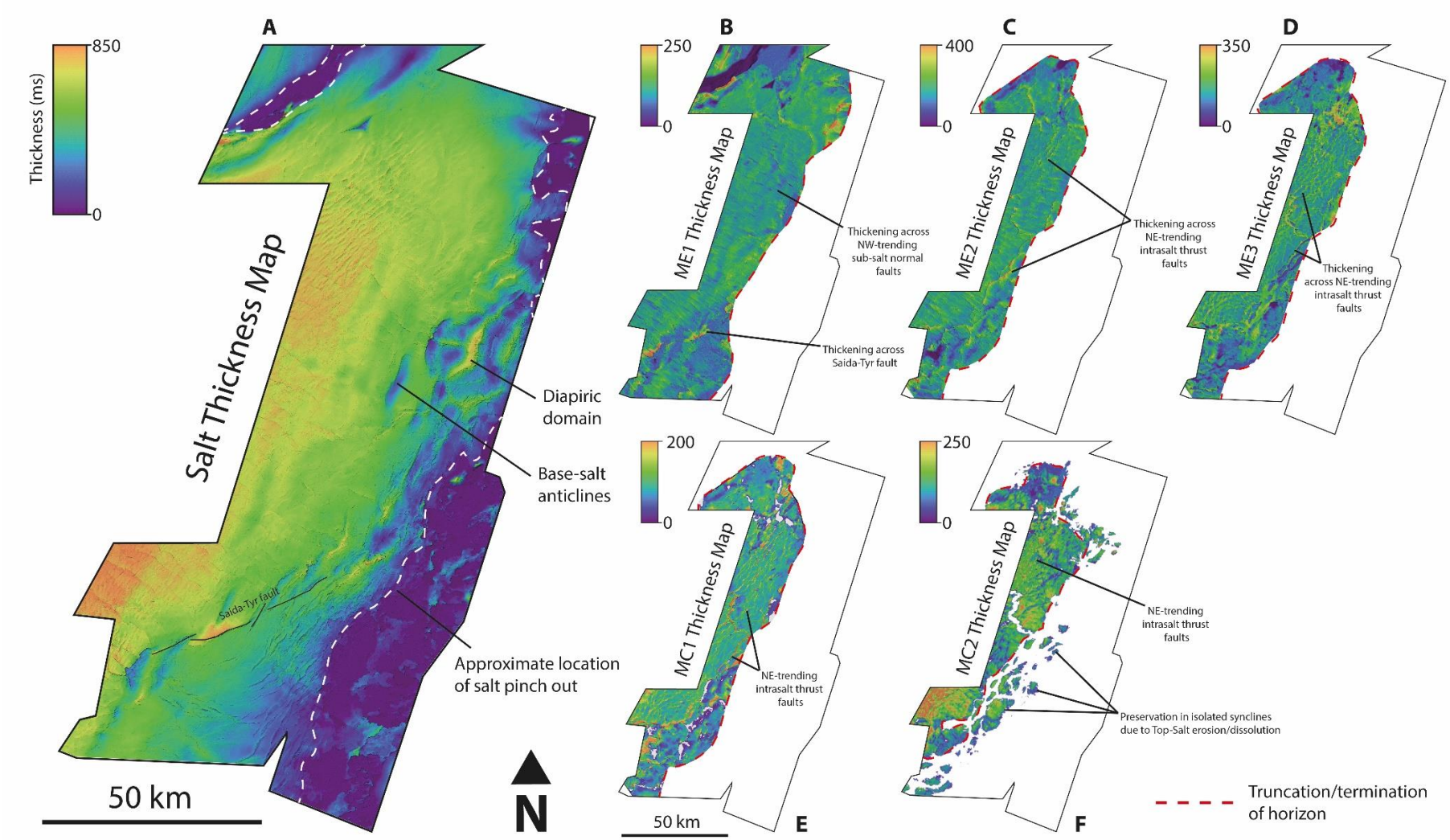

800 **Fig 10** (A) Total salt thickness map showing basinward thickening and pinch-out updip. (B-F) Annotated thickness maps of individual intrasalt units within
801 the contractional domain.

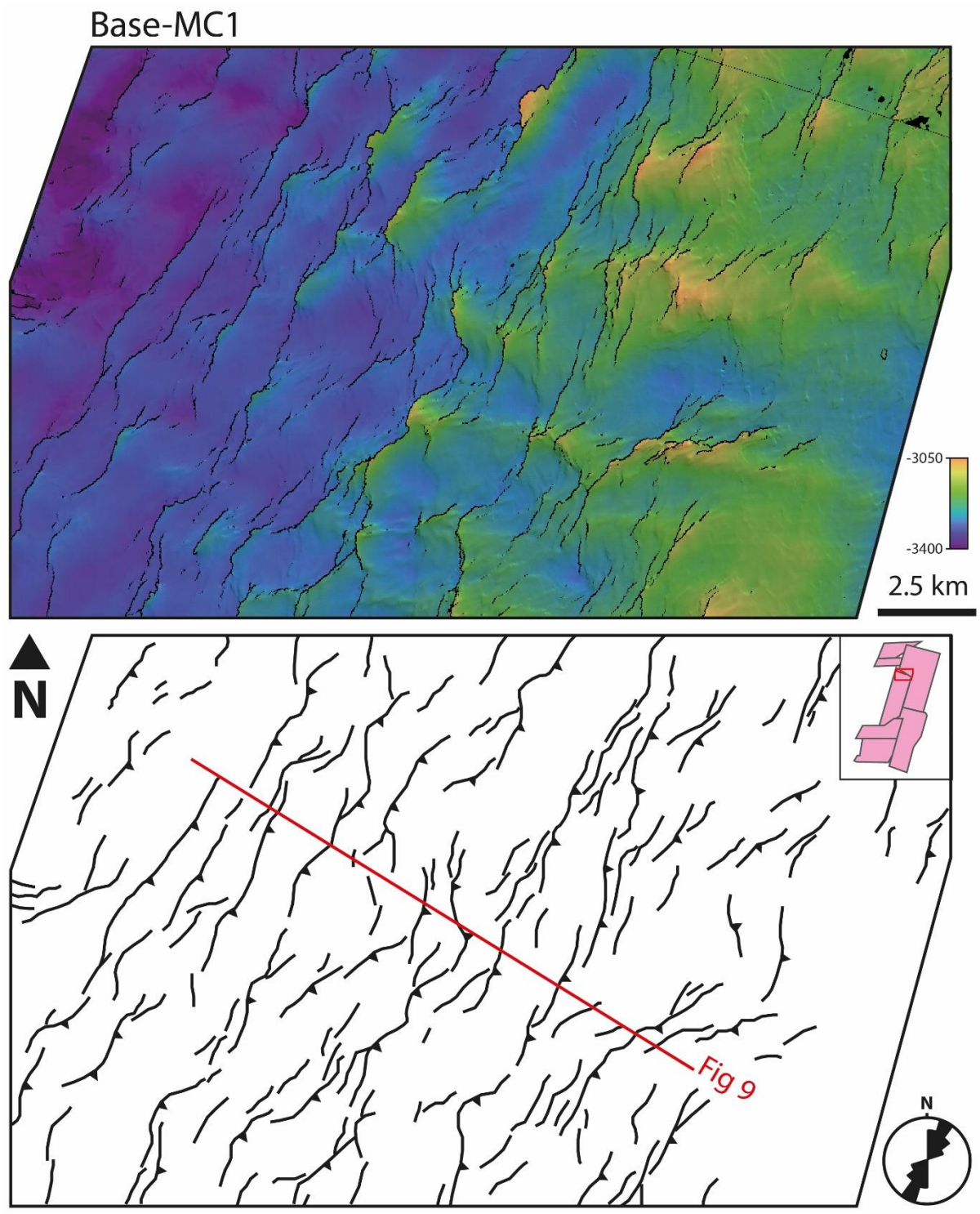

802 **Figure 11** Detailed structure map of Base-MC1 (Top-ME2) reflection showing dominant NNE
803 structural trend of intrasalt faults and folds. Rose diagram and location shown in inset.

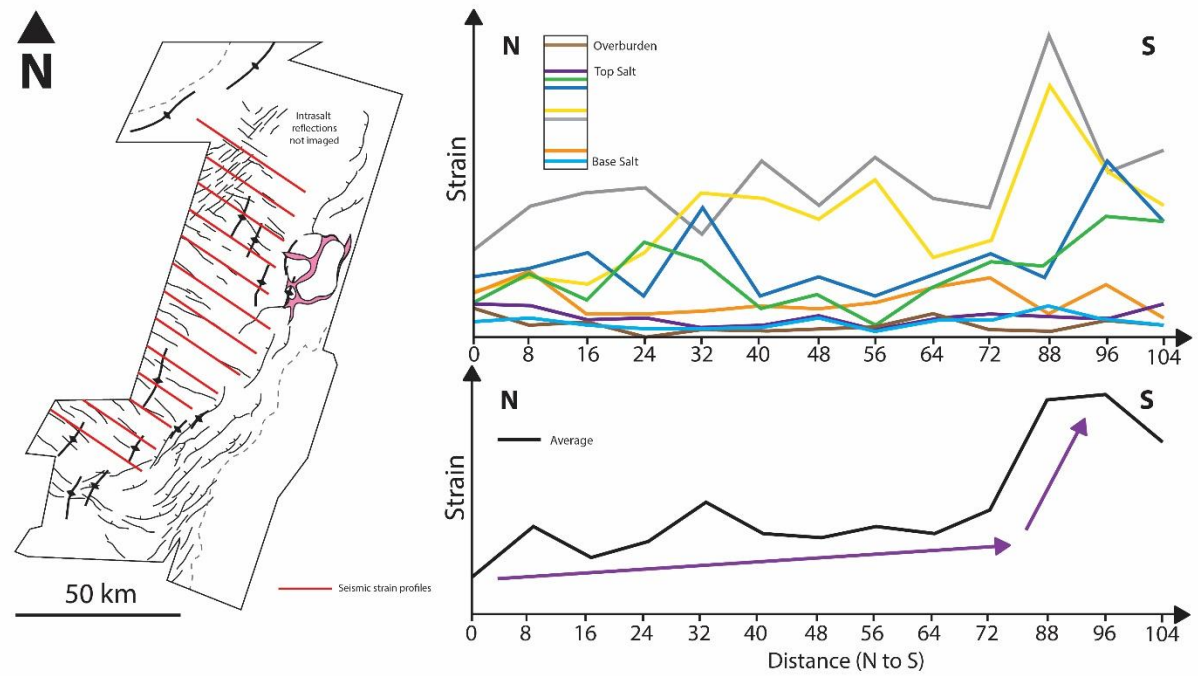

804 **Figure 12** (A) Location of 2D seismic sections used in strain measurements. (B) Lateral seismic strain
805 variations plotted along margin (North to South) calculated for individual intrasalt reflections (upper)
806 and average across all reflections (lower). Red arrows indicate overall trend of strain increasing toward
807 the South.

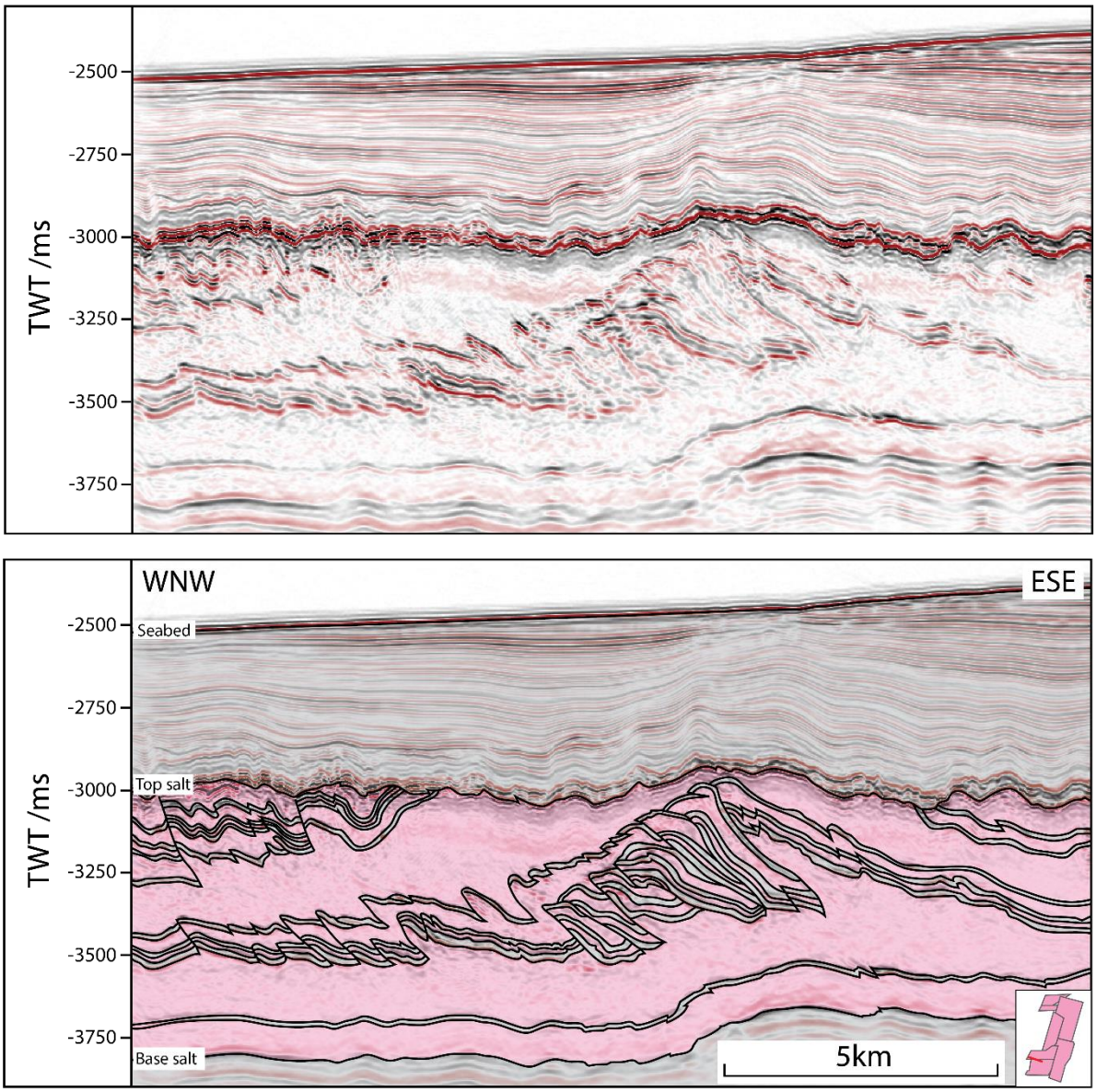

808 **Figure 13** Seismic section (upper) and interpretation (lower) showing kilometre-scale thrust duplex
809 accommodating very high strain over relatively short distance. MC2 reflections truncated at the top-
810 salt. Note very low strain on Top-ME1 reflection. Location shown in inset and Figures 6 and 7.

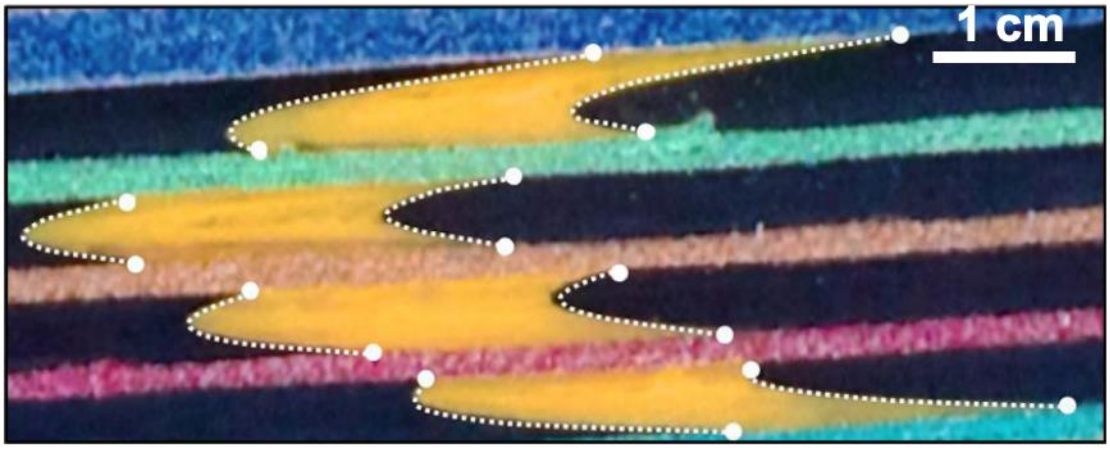

811 **Figure 14** Physical model using silicone as salt analogue demonstrating overall Poiseuille flow, with
812 passive strain markers (yellow) showing higher strains in ductile silicone layers than intervening brittle
813 sand layers (Weijermars and Jackson, 2014).

814

815

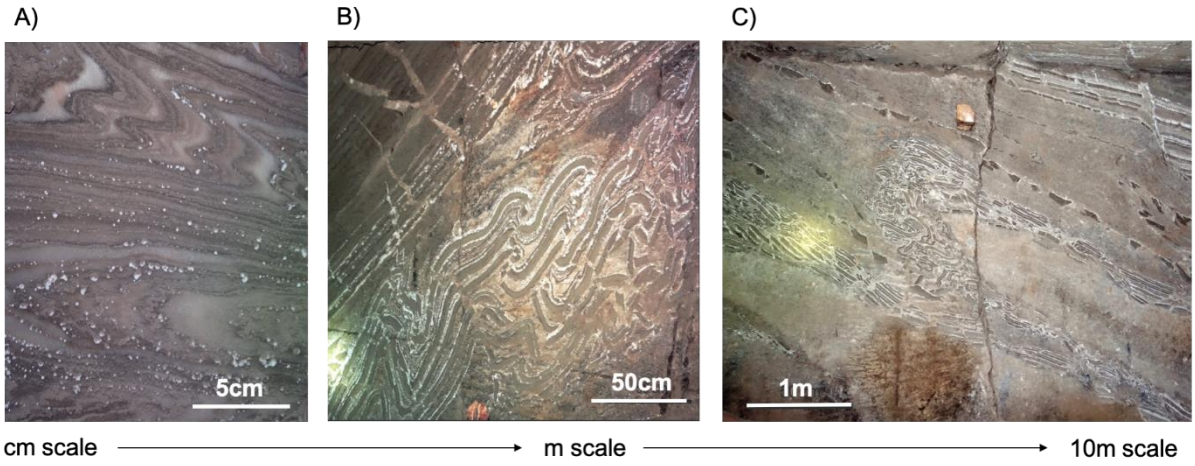

816 **Figure 15** Structures exposed in the Wieliczka Salt Mine in Poland show different ways in which strain
817 is accommodated by different units depending on their physical properties (e.g. viscosity), thickness
818 and position in the sequence. Modified from Burliga et al. (2018).

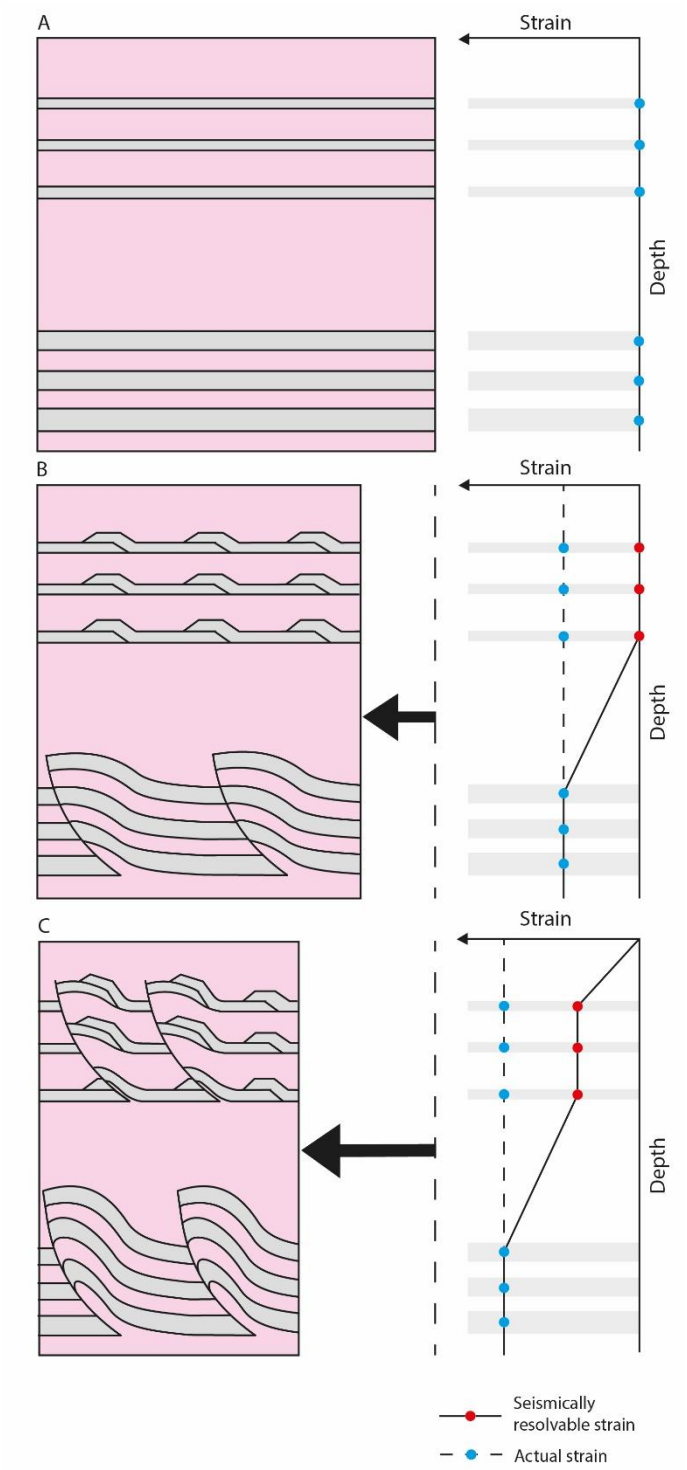

819 **Figure 16** Schematic cartoon showing evolution of strain within a heterogeneous salt sheet. (A)
820 Undeformed brittle intrasalt units within halite-rich ductile sequence. (B) The upper unit with a lower
821 brittle:ductile ratio accommodates shortening via small, sub-seismic structures while the lower unit
822 with a higher brittle:ductile ratio develops seismically-resolvable thrust faults. (C) The upper unit
823 accommodates strain on two new, seismically-resolvable thrust faults while the lower unit
824 accommodates strain with slip on pre-existing structures. The result is that the upper unit appears less
825 strained on seismic data than the lower unit, despite both having accommodated the same magnitude
826 of shortening.

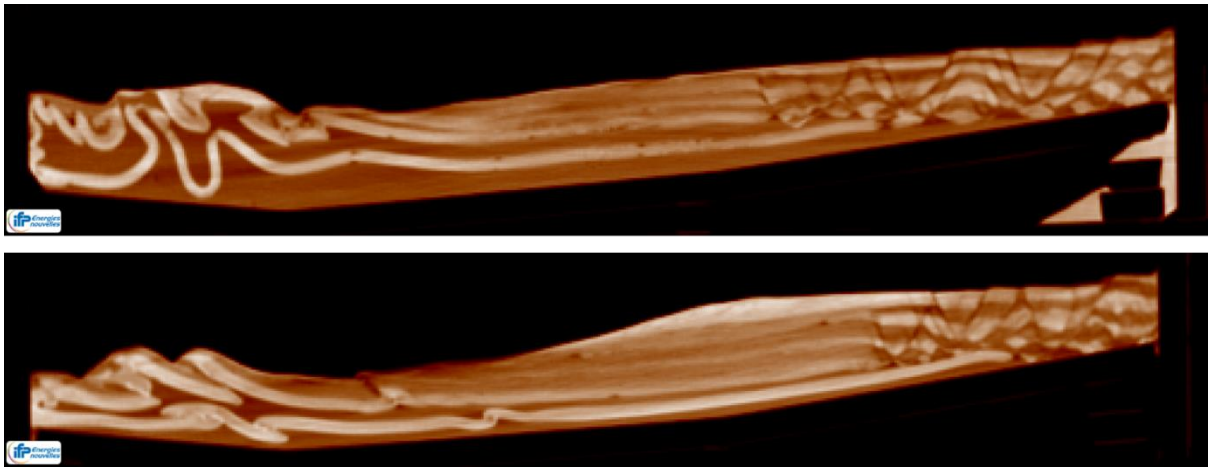

Figure 17 Cross sectional CT scans of physical analogue models of salt tectonics on a passive margin. The interbedded sand layer deforms in a ductile manner when encased in thick silicone (upper) and in a brittle manner when encased in thin silicone (lower). Models run at IFP Energies Nouvelles, Paris.

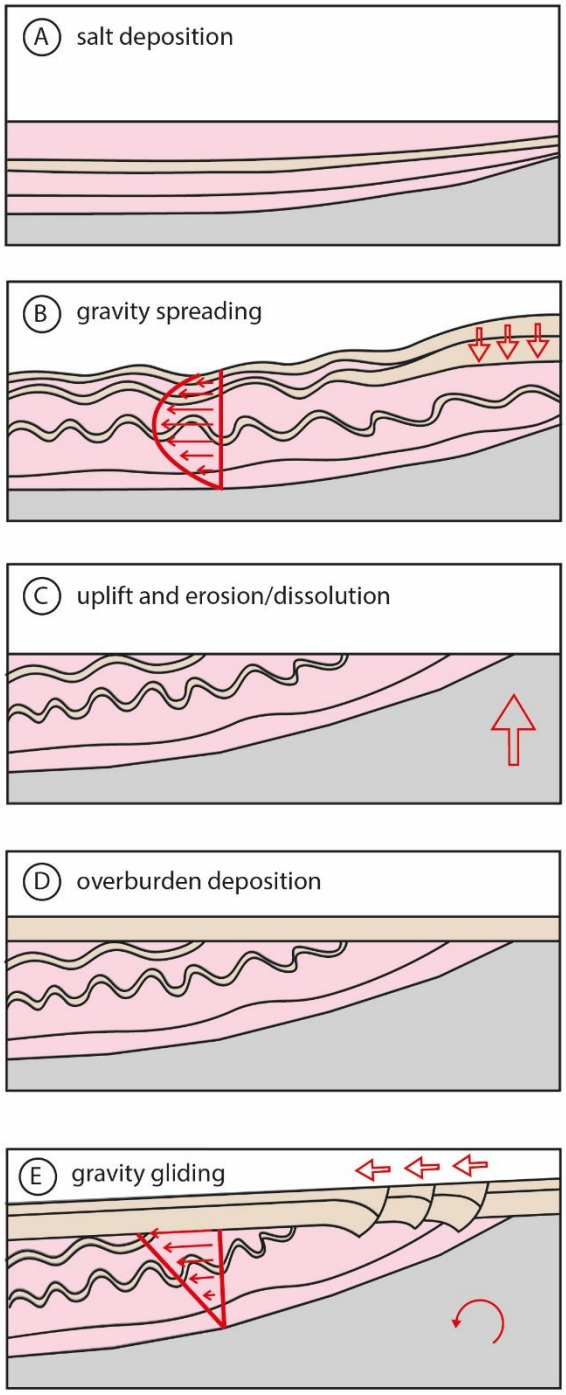

Figure 18 Schematic structural evolution of the salt deformation on the Levant margin. (A) Deposition of salt layers, thinning updip toward the shelf. (B) Thick sediments on shelf are deposited contemporaneously with upper brittle intrasalt units, resulting in gravity spreading due to pressure difference and basinward Poiseuille flow. The middle intrasalt units accommodate more shortening than upper and lower units where drag against top- and base-salt hinders basinward flow. (C) Uplift of the Levant margin causes erosion and dissolution of the sediments and salt layers updip. (D) Basin subsidence resumes and an overburden is deposited on top of the deformed salt sheet. (E) Greater subsidence in the deep basin causes margin tilt and gravity gliding is initiated, resulting in a drag-induced basinward Couette flow.

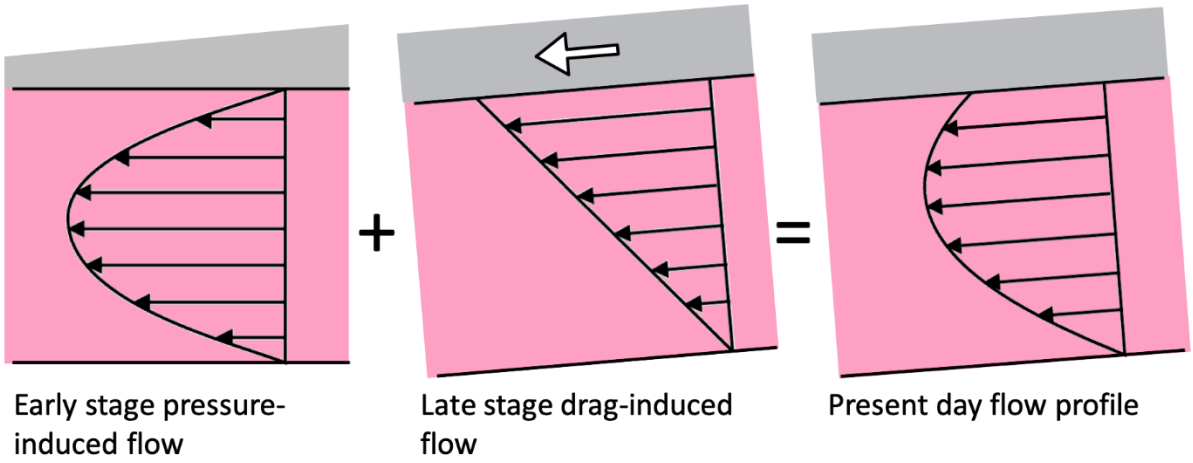

Figure 19 Summing the strain resulting from an early pressure-induced Poiseuille flow followed by a later drag-induced Couette flow results in an asymmetric Poiseuille flow profile.

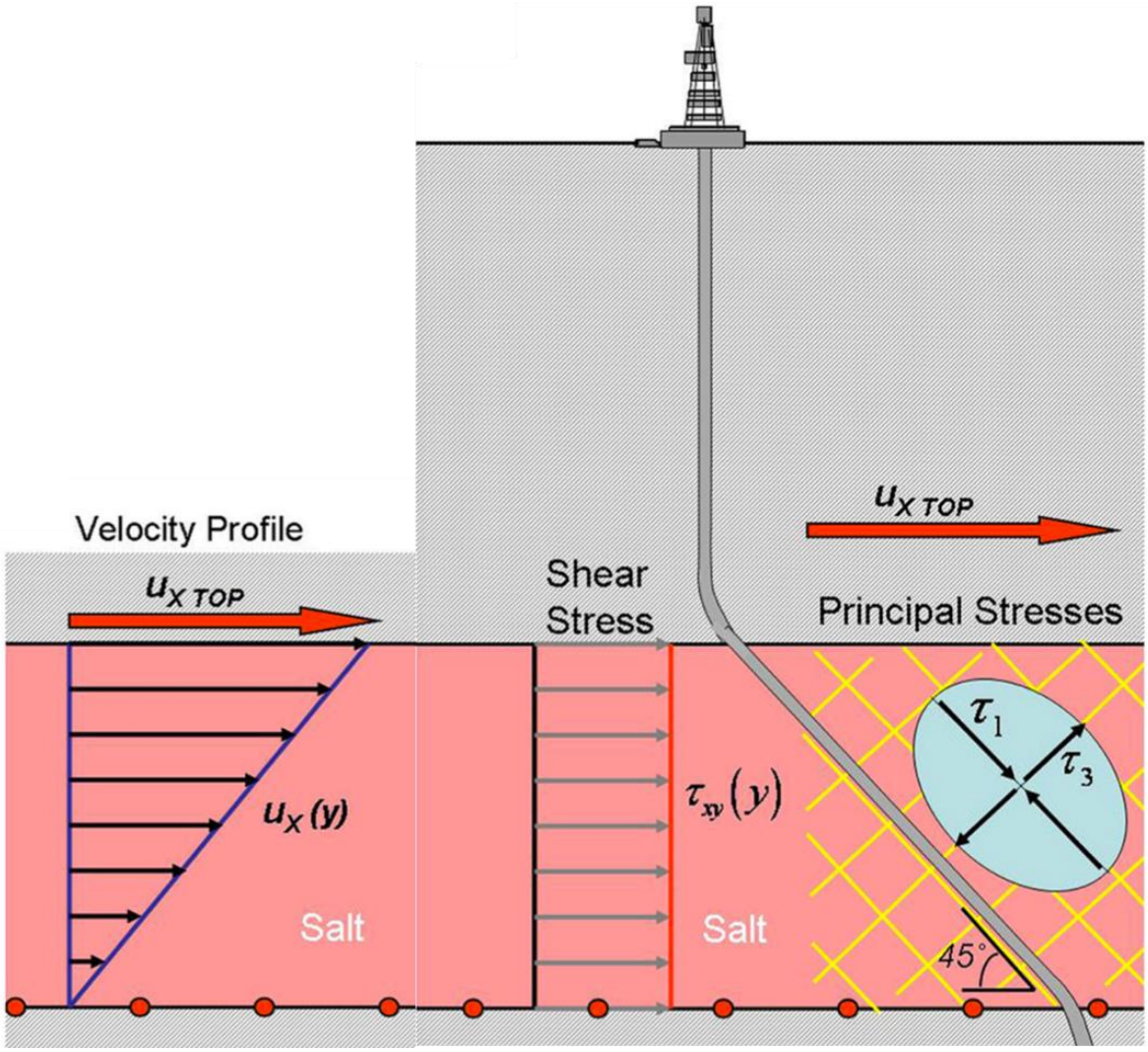

841 **Figure 20** Optimal drilling trajectory through a salt sheet deforming via Couette flow in order to
842 minimise shear stresses acting on the well bore. Peak shear stress of salt layers having Couette flow
843 can be mitigated by drilling at 45° to the direction of flow in the salt layer. Modified from Weijermars
844 et al. (2014).